

DeepWiener: Neural Networks for CMB polarization maps and power spectrum computation

Belén Costanza,^{a,b,1} Claudia G. Scóccola,^c Matías Zaldarriaga^d

^aFacultad de Ciencias Astronómicas y Geofísicas, Universidad Nacional de La Plata, Observatorio Astronómico, Paseo del Bosque, B1900FWA La Plata, Argentina

^bConsejo Nacional de Investigaciones Científicas y Técnicas (CONICET), Rivadavia 1917, Buenos Aires, Argentina

^cDepartamento de Física, FCFM, Universidad de Chile, Blanco Encalada 2008, Santiago, Chile

^dSchool of Natural Sciences, Institute for Advanced Study, 1 Einstein Drive, Princeton, NJ 08540, USA

E-mail: belen@fcaglp.unlp.edu.ar, claudia.scoccola@uchile.cl, matiasz@ias.edu

Abstract. To study the early Universe, it is essential to estimate cosmological parameters with high accuracy, which depends on the optimal reconstruction of Cosmic Microwave Background (CMB) maps and the measurement of their power spectrum. In this paper, we generalize the neural network developed for applying the Wiener Filter, initially presented for temperature maps in previous work, to polarization maps. Our neural network has a UNet architecture, including an extra channel for the noise variance map, to account for inhomogeneous noise, and a channel for the mask. In addition, we propose an iterative approach for reconstructing the E and B-mode fields, while addressing the E-to-B leakage present in the maps due to incomplete sky coverage. The accuracy achieved is satisfactory compared to the Wiener Filter solution computed with the standard Conjugate Gradient method, and it is highly efficient, enabling the computation of the power spectrum of an unknown signal using the optimal quadratic estimator. We further evaluate the quality of the reconstructed maps at the power spectrum level along with their corresponding errors, finding that these errors are smaller than those obtained using the well-known pseudo- C_ℓ approach. Our results show that increasing complexity in the applied mask presents a more significant challenge for B-mode reconstruction.

¹Corresponding author.

Contents

1	Introduction	1
2	Methodology	3
2.1	Wiener Filter and loss function	3
2.2	Power spectrum estimation	6
3	DeepWiener	8
4	Datasets	9
5	Results	12
5.1	Comparison with PCG results	12
5.2	Implementation of the power spectrum	15
5.3	Comparison with pseudo- C_ℓ estimator	20
6	Conclusion	23
A	Conjugate gradient algorithm	24
B	Partial sky polarization	25
C	Neural network iterations	26
D	Computation time	27

1 Introduction

The Cosmic Microwave Background (CMB) is one of the richest sources of information for understanding the origin and evolution of our Universe. This relic radiation was released soon after the recombination epoch, when the Universe was 380,000 years old. Precise measurements of the CMB temperature and polarization anisotropies allow for accurate estimation of the cosmological parameters, helping to constrain current cosmological models.

Primordial metric perturbations can be split into scalar and tensor types, simplifying the equations for the evolution of the perturbations in matter and in radiation temperature and polarization. While both scalar and tensor perturbations source temperature anisotropies, CMB polarization shows a distinct behavior: decomposing polarization into gradient (E-modes) and curl (B-modes) components reveals that E-modes receive contributions from both scalar and tensor perturbations, whereas B-modes arise exclusively from primordial gravitational waves (tensor perturbations) [1]. The CMB polarization pattern has been measured by satellite-based experiments like, WMAP [2, 3] and Planck [4, 5], as well as ground-based experiments, like ACT [6, 7] and SPTpol [8], specifically the E-mode polarization with high accuracy.

Measurements of B-mode polarization remain challenging yet are crucial, as they provide direct information about the stochastic background of gravitational waves left over from the inflationary epoch. This constitutes a major goal of cosmology, enabling constraints

on cosmological models and offering insight into the inflationary energy scale. Future and on-going experiments, like Lite-Bird [9], PICO [10], SPT-3G [11], Simons Observatory [12], CMB-S4 [13], and QUBIC [14–16], with a large number of highly sensitive detectors, attempt to measure the B-mode polarization.

The emergence of new experiments with ambitious technological requirements, together with the increasing volume of CMB data they will provide, demands the development of sophisticated tools to maximize the extraction of cosmological information. There are three essential data compression stages in a CMB pipeline: the conversion of raw time-ordered data (TOD) into a sky map (map making), the estimation of the power spectra, and the inference of cosmological parameters [17]. At each stage, the dataset is compressed to a more manageable size. To ensure that no significant cosmological information is lost, every step must be carefully optimized for both accuracy and computational efficiency.

In this context, we address the challenge of optimal reconstruction of polarization maps and power spectrum estimation using noisy and sparse data. The well-known Wiener Filter (WF) [18] is the optimal filter for noise reduction in these maps and for reconstructing the underlying signal [19], as it minimizes the residual variances in the reconstruction of the true field from noisy observations. For the CMB, which is a Gaussian distributed field, the WF solution maximizes the posterior probability of the signal given the data [20].

However, the computational demands for deriving the exact WF solution have increased significantly due to the vast amount of data involved. Additionally, calculating the WF matrix requires inverting the covariance matrices of both signal and noise, where the signal covariance is diagonal in Fourier space, while the noise covariance is diagonal in configuration space. Then, the combined covariance is neither diagonal nor sparse in any basis. One approach to solving the WF is to employ a conjugate gradient method for matrix inversion with an effective preconditioner [21], which is a complicated task as it must approximate the true inverse while maintaining sparsity. Examples of preconditioners include the inverse of the diagonal part of the matrix [22] or the multigrid preconditioner [23], among others. Other methods without preconditioners include the incorporation of a messenger field between bases [24, 25].

For this reason, in this paper, we attempt to simulate the WF considering Deep Learning techniques, since neural networks have proven effective in various cosmological analysis [26, 27]. After that, we proceed to estimate the power spectrum, as we have done on temperature maps [28], but generalized to polarization, implementing an optimal quadratic estimator approach suggested by [29, 30], obtained from the maximization of the likelihood. The use of neural networks to simulate the WF allows to compute a simulation-based optimal quadratic estimator, as the trained models are more efficient for performing the WF compared to the Conjugate Gradient method, which can become prohibitively expensive in certain cases.

Due to foreground contamination from the galactic plane, the local Universe, and extragalactic sources in CMB observations, experiments typically measure a partial CMB sky by applying a binary mask to the full-sky map. One complication that arises from incomplete sky coverage is the transmission of power from the E-mode to the B-mode, a problem commonly referred to as E-to-B leakage. Additionally, since the B-component is expected to be at least an order of magnitude smaller than the E-component, a clean separation of the modes is necessary. Several approaches have tried to mitigate the E-to-B leakage in partial sky analysis. Some of these focus on separating the contributions of the E and B *pure* components from the *ambiguous* modes, which cause the E-to-B leakage, by finding the orthonormal bases for these three components [31], or by using the pure pseudo- C_ℓ formalism [32]. Other approaches attempt to mitigate the E-to-B leakage at the power spectrum level using deep

learning techniques [33].

In this work, we address the challenge of applying the WF to polarization maps while simultaneously dealing with E-to-B leakage. We start by obtaining the WF for the E-mode, as the Q and U maps predominantly consist of E-modes due to their stronger signal. We then create a new dataset by removing the contribution of the E-mode WF, allowing the network to focus on the B-modes. This approach is motivated by [34] where the modes decomposition is considered as an application of the WF. If one can identify and remove the E-mode contribution from the data, it will not interfere with the WF of the B-mode.

We have adapted the WienerNet neural network [35], originally developed for homogeneous noise, to handle inhomogeneous noise in temperature maps by incorporating an additional channel with an inhomogeneous variance map, as introduced in our previous work [28]. As demonstrated in that work, the WF predictions after model training are highly efficient. In this work, we proceed to estimate the wiener filtered map and the power spectrum of the polarization field and its covariance matrix. Our code is implemented in TENSORFLOW 2 and KERAS, using PYTHON 3.

In this paper, we focus on polarization maps and present a method for reconstructing the E- and B-mode fields, accounting for realistic inhomogeneous noise and varying coverage complexities. Our aim is to provide a practical framework for current and future experiments, as the Q & U Bolometric Interferometer for Cosmology (QUBIC) experiment, which has a multi-peak synthesized beam [16] that lead to spectro-imaging with spatial and subfrequency correlations.

This paper is organized as follows: In section 2 we described the basics of Wiener filter and power spectrum estimation, with the loss functions implemented in this work. In section 3 we present the neural network architecture developed for our purposes called DeepWiener. In section 4 we explain how we created the necessary datasets with the different masks applied and noise properties. Then, in section 5 we presents the neural network results of the E and B-modes compared with the WF using a conjugate gradient method, together with the power spectrum estimation of both modes. In addition, in the same section we compare our framework with the pseudo- C_ℓ approach. The discussion and conclusions are presented in section 6.

2 Methodology

In this section, we introduce the Wiener filter and the methodology adopted to implement it using neural networks. Additionally, we provide an overview of the algorithm used to estimate the power spectra of CMB polarization maps (E-mode power spectrum and B-mode power spectrum) after applying the Wiener filter.

2.1 Wiener Filter and loss function

The Wiener Filter is the optimal filter to enhance signal quality by reducing the noise present on gaussian fields, as in the case of the CMB signal. Moreover, for CMB observations, the data is a linear transformation of the initial modes. Hence, let us suppose that the measurements \mathbf{d} are a linear combination of the underlying field \mathbf{s} that we want to estimate:

$$\mathbf{d} = \mathbf{R}\mathbf{s} + \epsilon, \tag{2.1}$$

where \mathbf{R} is the response matrix of the measurement procedure and ϵ is the data uncertainty.

The application of a filter, mathematically expressed as a convolution, establishes a linear connection between the reconstructed underlying signal $\hat{\mathbf{s}}_{WF}$ and the input data \mathbf{d} , such that $\hat{\mathbf{s}}_{WF} = M\mathbf{d}$. The matrix M is determined by minimizing the variance of the residuals between the reconstructed signal and the true underlying signal. In the case of Gaussian random fields, this result coincides with the Bayesian estimator that maximizes the conditional probability of the signal given the data:

$$P(\mathbf{s}|\mathbf{d}) \propto \exp \left[-\frac{1}{2}(\mathbf{s}^\dagger \mathbf{S}^{-1} \mathbf{s} + (\mathbf{d} - \mathbf{R}\mathbf{s})^\dagger \mathbf{N}^{-1} (\mathbf{d} - \mathbf{R}\mathbf{s})) \right], \quad (2.2)$$

where \mathbf{S} and \mathbf{N} are the covariance matrices of the signal and noise, respectively. Maximizing this conditional probability is equivalent to minimizing the function:

$$\chi^2(\mathbf{s}) = \mathbf{s}^\dagger \mathbf{S}^{-1} \mathbf{s} + (\mathbf{d} - \mathbf{R}\mathbf{s})^\dagger \mathbf{N}^{-1} (\mathbf{d} - \mathbf{R}\mathbf{s}). \quad (2.3)$$

which results in the Wiener Filter estimator:

$$\hat{\mathbf{s}}_{WF} = \mathbf{S}(\mathbf{S} + \mathbf{N})^{-1} \mathbf{R}^{-1} \mathbf{d} = (\mathbf{S}^{-1} + \mathbf{R}^\dagger \mathbf{N}^{-1} \mathbf{R})^{-1} \mathbf{R}^\dagger \mathbf{N}^{-1} \mathbf{d}. \quad (2.4)$$

To compute this exact WF estimator, the expression (2.4) is written as a linear system and inverted through the Preconditioner Conjugate Gradient (PCG) algorithm. In this work, we compare the performance of the neural network predictions with the WF results obtained using the PCG method. For detailed information about the PCG algorithm, refer to Appendix A.

For training a neural network to simulate the WF, it is natural to choose the same expression as in equation (2.3) for the loss function:

$$J(d, y) = \frac{1}{2}(y - d)^T N^{-1}(y - d) + \frac{1}{2}y^T S^{-1}y, \quad (2.5)$$

where y is the output of the neural network that represents the reconstructed signal, d is the noisy data (Q_{obs} and U_{obs}), and N and S are the covariance matrices associated with noise and signal, respectively. The implementation for polarization maps is:

$$J_{Q,U} = \sum_i^{N_{pix}} \frac{(Q_{NN} - Q_{obs})^2}{\sigma_i^2} + \frac{(U_{NN} - U_{obs})^2}{\sigma_i^2} + \sum_l \frac{E_{lNN} E_{lNN}^*}{C_l^E} + \frac{B_{lNN} B_{lNN}^*}{C_l^B}, \quad (2.6)$$

where Q_{obs} and U_{obs} are the inputs of the neural network, Q_{NN} and U_{NN} are the predictions, σ_i^2 is the pixel noise variance, and the Fourier terms are evaluated in the (E, B) basis. These expressions are the same as the ones presented in [35].

We aim to extract the E_{WF} and B_{WF} components from Q_{WF} and U_{WF} . In order to address the challenge of the E-to-B leakage, we performed the optimization of these components separately and iteratively, in a series of steps.

First, we built the observed polarization maps $Q_{obs}^{(1)}$ and $U_{obs}^{(1)}$ with inhomogeneous noise and mask applied. Then, we trained the neural network and obtained $Q_{NN}^{(1)}$ and $U_{NN}^{(1)}$ as outputs, which gave us $E_{NN}^{(1)}$ and $B_{NN}^{(1)}$ after the appropriate transformation in Fourier space for the partial sky, which is explained in Appendix B. Since the B-mode is a weak signal compared to the E-mode, the neural network primarily captures the Wiener Filter of the E-mode but almost nothing of the B-mode.

When the loss function $J_{Q,U}$ in equation (2.6) is correctly minimized, the outputs of the neural network should correspond to the WF of Q and U , which are then transformed into E_{WF} and B_{WF} . In practice, however, the optimization of the neural network provides an approximation to the WF. Specifically, during the initial training, we can accurately reconstruct the E-mode contribution, but struggle with the B-mode, as the network fails to accurately isolate the *ambiguous* modes from the *pure* ones.

Several implementations could affect the optimization of a neural network, we do not discard the possibility of finding even better results by expanding the set of hyperparameters tested or considering different initializations, at the expense of more computing time for training. In addition, this architecture is written in an updated version of TENSORFLOW in order to be used in PYTHON 3 and with the new GPUs drivers. The WienerNet network (in which our network is based) was written in TENSORFLOW 1 and the B-modes were obtained at the first training, indicating some differences in the internal implementations of the TENSORFLOW library that could affect the search of an optimal solution.

Therefore, we propose a method to extract as much of the E-mode contribution from the data as possible, removing it afterward to avoid contaminating the WF for the B-mode. Subsequently, we generate a new dataset with the E-mode contribution removed:

$$Q_{obs}^{(2)} = \left(Q_{obs} - Q_{ENN}^{(1)} \right) \quad (2.7)$$

$$U_{obs}^{(2)} = \left(U_{obs} - U_{ENN}^{(1)} \right), \quad (2.8)$$

where $Q_{ENN}^{(1)}$ and $U_{ENN}^{(1)}$ are the E-mode contributions of the first neural network outputs. This new dataset has a lower contribution of the E-mode in $Q_{obs}^{(2)}$ and $U_{obs}^{(2)}$, reducing the leakage present in the B-mode.

We trained the neural network again with these residuals using the loss function $J_{Q,U}$, equation (2.6), which now takes the form:

$$J_{Q,U} = \sum_i^{N_{pix}} \frac{\left(Q_{NN}^{(2)} - Q_{obs}^{(2)} \right)^2}{\sigma_i^2} + \frac{\left(U_{NN}^{(2)} - U_{obs}^{(2)} \right)^2}{\sigma_i^2} + \sum_l \frac{E_{lNN} E_{lNN}^*}{C_l^E} + \frac{B_{lNN} B_{lNN}^*}{C_l^B}, \quad (2.9)$$

where we added the contribution $E_{NN}^{(1)}$ to the Fourier E-mode term, as C_l^E represents the total power spectrum. Afterward, we obtained $Q_{NN}^{(2)}$ and $U_{NN}^{(2)}$ as outputs. Since $Q_{obs}^{(2)} = Q_{obs} - Q_{ENN}^{(1)}$, it follows that $Q_{NN} = Q_{NN}^{(2)} + Q_{ENN}^{(1)}$, and $(Q_{NN}^{(2)} - Q_{obs}^{(2)}) = (Q_{NN} - Q_{obs})$.

Then, we can further reduce the leakage by creating new maps with almost no E-mode contribution:

$$Q_{obs}^{(3)} = (Q_{obs} - Q_{ENN}^{(1)} - Q_{ENN}^{(2)}) \quad (2.10)$$

$$U_{obs}^{(3)} = (U_{obs} - U_{ENN}^{(1)} - U_{ENN}^{(2)}). \quad (2.11)$$

Finally, if we use the maps $Q_{obs}^{(3)}$ and $U_{obs}^{(3)}$, the contribution now is primarily from the B-mode rather than the E-mode. The outputs of the neural network with these maps is $Q_{NN}^{(3)}$ and $U_{NN}^{(3)}$, which allow us to obtain the Wiener Filter of the B-mode. Besides, it is possible to use the results from the iterations to further improve the Wiener Filter of the E-mode, obtaining the E-mode contribution from $Q_{NN} = Q_{ENN}^{(1)} + Q_{ENN}^{(2)} + Q_{NN}^{(3)}$ and $U_{NN} = U_{ENN}^{(1)} + U_{ENN}^{(2)} + U_{NN}^{(3)}$. This iterative process can be repeated as many times as needed to achieve better performance.

On the other hand, when we obtain observed maps Q and U with minimal E-mode contribution, we can assume that the polarization information comes predominantly from the B-mode contribution, therefore the transformation from spin-2 quantities Q and U to scalar quantities will yield an E-mode map nearly zero. Thus, we can treat the problem similarly to the temperature case where the neural network was trained with a temperature map as input; in this case it would be a B-mode map. Then, instead of training the neural network with $Q_{obs}^{(3)}$ and $U_{obs}^{(3)}$ using the loss function $J_{Q,U}$, we can train using the B-mode map, $B_{obs}^{(3)}$, that is derived from the observed maps $Q_{obs}^{(3)}$ and $U_{obs}^{(3)}$ considering the following loss function:

$$J_B = \sum_i^{N_{pix}} \frac{(B_{NN} - B_{obs}^{(3)})^2}{\sigma_i^{*2}} + \sum_\ell \frac{B_{lNN} B_{lNN}^*}{C_l^B}. \quad (2.12)$$

It is important to note that the noise variance map σ^2 for Q and U maps is not the same as the noise variance map σ^{*2} for E and B maps. We can approximate σ^{*2} by computing the variance in each pixel of the difference $B_{obs} - B_{sky}$ over thousands of simulations, as described in the section 4, where B_{obs} is derived from Q_{obs} and U_{obs} . The output of the neural network will directly provide the WF of the B-mode, and in this case, fewer iterations are required compared to those needed when using the loss function $J_{Q,U}$, as explained in section 5.

This expression is not derived from (2.6) but rather is an approximation where the B-mode map is not contaminated by *ambiguous* modes and the σ^{*2} is estimated through simulations.

2.2 Power spectrum estimation

In CMB data analysis, it is of interest to compress the information in the field into a summary statistic, such as the power spectrum. After reconstructing the underlying signal $\hat{\mathbf{s}}$ using a neural network that efficiently simulates the optimal WF method, we aim to obtain the power spectrum amplitudes (or band-powers Θ if binned) and their covariance matrix using the optimal quadratic estimator. For that purpose, we follow the approach outlined in [29, 30].

To find the most probable set of band-power Θ given the measurements \mathbf{d} , we need to maximize the likelihood function $L(\mathbf{d}|\Theta)$, which is proportional to the posterior $P(\Theta|\mathbf{d})$ assuming a flat prior on Θ . Since the modes are Gaussian distributed, the likelihood function can be expressed as:

$$L(\mathbf{d}|\Theta) = (2\pi)^{-N/2} \det(C)^{-1/2} \exp\left(-\frac{1}{2} \mathbf{d}^\dagger C^{-1} \mathbf{d}\right), \quad (2.13)$$

where the covariance matrix of the data can be expressed as a linear sum over the band-powers, with their response matrix P_ℓ for each mode:

$$C = \mathbf{R} \mathbf{S} \mathbf{R}^\dagger + \mathbf{N} = \sum_\ell \Theta_\ell P_\ell + \mathbf{N}. \quad (2.14)$$

The maximum of the likelihood (2.13) is the optimal quadratic estimator, obtained using Newton's method:

$$F_{\ell\ell'} \Theta_\ell = \frac{1}{2} \mathbf{d}^\dagger C^{-1} P_{\ell'} C^{-1} \mathbf{d} - \frac{1}{2} \text{Tr}[C^{-1} P_{\ell'} C^{-1} \mathbf{N}], \quad (2.15)$$

where F^{-1} is the local estimate of the covariance matrix of the band-power parameters,

$$F^{-1} = \langle \Theta \Theta^\dagger \rangle - \langle \Theta \rangle \langle \Theta^\dagger \rangle. \quad (2.16)$$

In practice, this analytical expression for the likelihood is inefficient, as its evaluation requires inversion or computing the determinant of a large, non-sparse matrix. Therefore, in our approach, we first worked with the variables \mathbf{s} , solving the WF with the neural network, and then marginalized over these variables to obtain the likelihood of the parameters.

To do so, we need to introduce a derivative matrix $\mathbf{\Pi}_\ell$ around some fiducial power spectrum \mathbf{S}^{fid} , defined as:

$$\left[\frac{\partial \mathbf{S}}{\partial \Theta_\ell} \right]_{\mathbf{S}^{\text{fid}}} = \mathbf{\Pi}_\ell. \quad (2.17)$$

Then, the true covariance can be written as:

$$\mathbf{S} = \mathbf{S}^{\text{fid}} + \sum_\ell \Delta \Theta_\ell \mathbf{\Pi}_\ell. \quad (2.18)$$

Note that for linear dependence of \mathbf{S} on Θ we can use

$$\mathbf{\Pi}_\ell = \frac{\mathbf{S}^{\text{fid}}}{\Theta_\ell}, \quad (2.19)$$

i.e. $\langle s_{k_\ell} s_{k_\ell}^* \rangle = \Theta_\ell \Pi_\ell(k_\ell)$, where, in this case, the derivative matrix take us from Θ_ℓ (the power spectrum value representative over a bin) to \mathbf{S} , which is the power spectrum.

Then, we expand the log-likelihood in terms of Θ to quadratic order around some fiducial values Θ_{fid} (marginalized over \mathbf{s}):

$$\ln L(\Theta_{\text{fid}} + \Delta \Theta) = \ln L(\Theta_{\text{fid}}) + \sum_\ell \left[\frac{\partial \ln L(\Theta)}{\partial \Theta_\ell} \right]_{\Theta_{\text{fid}}} \Delta \Theta_\ell + \frac{1}{2} \sum_{\ell \ell'} \left[\frac{\partial^2 \ln L(\Theta)}{\partial \Theta_\ell \partial \Theta_{\ell'}} \right]_{\Theta_{\text{fid}}} \Delta \Theta_\ell \Delta \Theta_{\ell'}, \quad (2.20)$$

where the last term of equation (2.20) defines the curvature matrix as the second derivatives of log-likelihood with respect to the parameters.

We define:

$$E_\ell(\mathbf{S}_{\text{fid}}, \hat{\mathbf{s}}) = \frac{1}{2} \hat{\mathbf{s}}^\dagger \mathbf{S}_{\text{fid}}^{-1} \mathbf{\Pi}_\ell \mathbf{S}_{\text{fid}}^{-1} \hat{\mathbf{s}} = \frac{1}{2} \sum_{k_\ell} \frac{\hat{s}_{k_\ell}^2}{\Theta_{\text{fid}, \ell} S_{\text{fid}, k_\ell}}, \quad (2.21)$$

where the sum over k_ℓ accounts for all the modes that contribute to the band-power Θ_ℓ . Then, the first derivative of the likelihood becomes:

$$\frac{\partial \ln L(\Theta)}{\partial \Theta_\ell} = E_\ell - b_\ell. \quad (2.22)$$

The maximum likelihood solution for $\hat{\Theta}$ is obtained setting the equation above equal to zero leading to the noise bias term equal to:

$$b_\ell = E_\ell(\Theta_{\text{fid}}, \hat{\mathbf{s}}_{s+n}), \quad (2.23)$$

where $\hat{\mathbf{s}}_{s+n}$ is the wiener-filtered map obtained from data that contains signal and noise ($s+n$), where the signal map is a realization of the *fiducial* power spectrum.

Finally, the peak of the likelihood function is obtained by setting the derivative of (2.20) with respect to $\Delta \Theta$ equal to zero, and using the equation (2.22), leading to:

$$(\mathbf{F} \Delta \Theta)_\ell = E_\ell - b_\ell, \quad (2.24)$$

where the signal map appearing in E_ℓ is a realization of the *true* power spectrum. This approach provides an unbiased estimator, as squaring the raw power spectrum requires subtracting the noise bias term. Additionally, the Fisher matrix accounts for both the covariance matrix and the band-power mixing, given that we are working with incomplete sky coverage in the signal estimation.

The bias term and the Fisher matrix are calculated with simulations of the *fiducial* power spectrum, and applying the WF to each of them. The estimation of the *true* power spectrum will be $\Theta_{fid} + \Delta\hat{\Theta}$.

In practice, the measurements consist of Q and U polarization maps, which are filtered through the neural networks models to obtain the maps Q_{WF} and U_{WF} , and subsequently E_{WF} and B_{WF} . Our goal is to estimate the auto-spectra of both the E-mode and B-mode, as these are rotationally invariant and thus more suitable for capturing the polarization information. Therefore, we need to compute equation (2.24) for each field:

$$(\mathbf{F}^E \Delta\Theta^E)_\ell = E_\ell^E - b_\ell^E, \quad (2.25)$$

$$(\mathbf{F}^B \Delta\Theta^B)_\ell = E_\ell^B - b_\ell^B, \quad (2.26)$$

and estimate the *true* power spectrum for each of them: $\Theta_{fid}^E + \Delta\hat{\Theta}^E$, $\Theta_{fid}^B + \Delta\hat{\Theta}^B$.

In section 5.3 we compare the uncertainties in the power spectrum estimation calculated with the procedure described above, with the power spectrum estimation using the NAMASTER library [36]. The last approach approximates the covariance matrix in equation (2.15) for its diagonal, assuming uncorrelated data. Some approximations and analytical expressions in flat-sky limit will be discussed and compared with our method in section 5.3.

3 DeepWiener

DeepWiener is the neural network developed to perform the WF on polarization data with inhomogeneous noise. The architecture presented in Figure 1 is the same as the one used for temperature maps with inhomogeneous noise in [28], originally based on WienerNet [35].

The architecture is an autoencoder Convolutional Neural Network (CNN), consisting of an encoder made up of convolutional layers and a decoder composed of transposed convolutional layers. This type of neural network is commonly used in image analysis for processing visual data. During the encoder phase, the network extracts key features from the input data while reducing its dimensions to form a latent space representation. Conversely, the decoder phase increases the layer dimensions to reconstruct an output image of the same size as the input.

This network follows a UNet architecture [37], but with two additional non-linear channels that operate on the mask and the variance map, while the linear channel is exclusively for the CMB maps. The outputs from the non-linear channel are multiplied by those from the map channel. This architecture is motivated by the need to perform linear operations on the CMB maps, as the WF is a linear filter applied to the data, as shown in equation (2.4).

The network receives as inputs the observed polarization maps, Q_{obs} and U_{obs} , with the corresponding mask applied and inhomogeneous noise added, assuming that the loss function $J_{Q,U}$ (equation (2.6)) is used. The outputs will be the filtered maps, Q_{WF} and U_{WF} . If the loss function J_B (equation (2.12)) is employed, the input consists of the observed B-mode map, which results from subtracting the E-mode contribution to the Q_{obs} and U_{obs} maps. In that case, the output is directly the filtered B-mode map, B_{WF} .

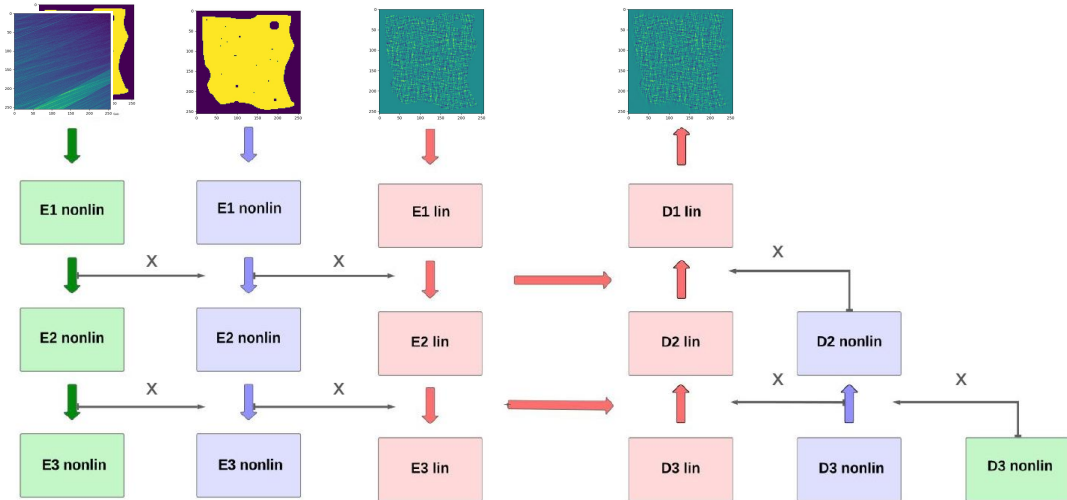


Figure 1. Scheme of DeepWiener architecture: only three encoders are presented for visualization. The black solid line represents the multiplication between channels, and the red arrow connecting the encoder part to the decoder part represents the skip connections in the linear channel. These skip connections are also present in the other channels although not being drawn here. The linear channel can be applied to the Q and U maps or the B mode map. The third channel is two-dimensional and contains both the variance map and the mask.

The key distinction from the procedure applied to temperature maps in [28] lies in addressing the E-to-B leakage present in polarization maps. To handle this, we created a new dataset with the E_{WF} contribution removed and retrained the neural network multiple times, each time removing the obtained E contribution, forcing the CNN to focus on the B-mode. This approach was motivated by the need to mitigate the *ambiguous* B-modes by enhancing the reconstruction of the E-modes that are present in the maps.

We have made the DeepWiener implementation and the power spectrum procedure publicly available in a dedicated GitHub repository¹.

4 Datasets

In this paper, we have built the training set considering polarization maps with inhomogeneous noise applied, as an extension of previous work with inhomogeneous noise but only on temperature maps. We adopt the flat-sky approximation and simulate maps of $20^\circ \times 20^\circ$ and 256×256 pixels. The angular resolution is determined by the size of the map and the number of pixels considered.

We extracted a map variance from Planck noise maps [4] to simulate the inhomogeneous noise to assess a realistic case, as illustrated in the left panel of Figure 2, while the distribution of variance levels among pixels is presented in the histogram of the right panel. Figure 3 presents the *fiducial* power spectrum of the E-mode and B-mode signal obtained

¹<https://github.com/Belencostanza/DeepWiener>

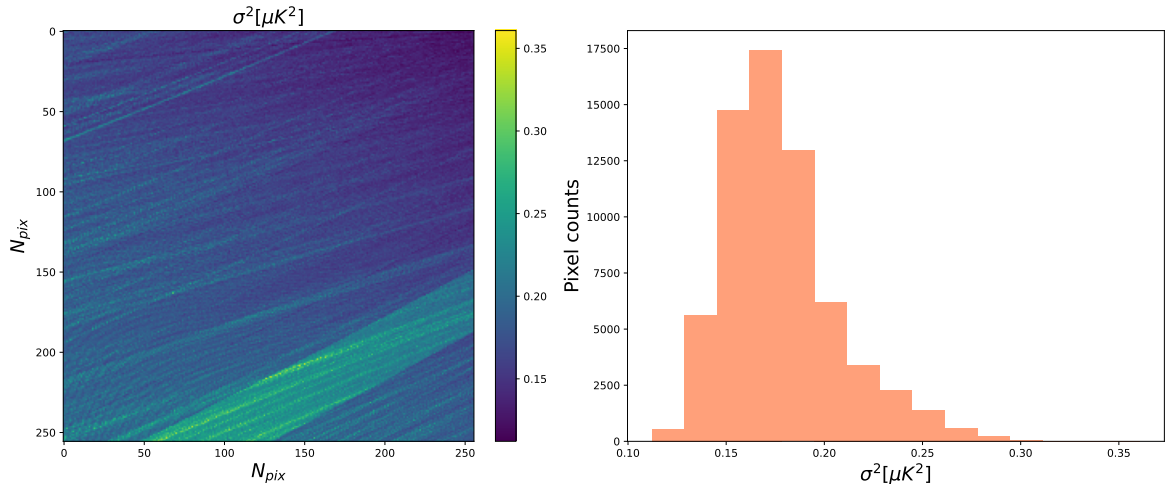


Figure 2. Left panel: Variance map extracted from Planck. Right panel: Histogram of the variance map showing the distribution of pixel counts across different noise variances.

using CAMB [38] with the cosmological parameters from the best fit of Planck data (2014) from Table 5 in [39]. In addition, it is presented the average noise level of the variance map, which cuts the B-mode power spectrum on scale $\ell \approx 1260$.

Initially, the neural network is trained with the observed Q and U maps to iteratively reconstruct the E -mode component, which is then subtracted from the observed maps. This process is repeated over several iterations until the E -mode contribution becomes negligible, leaving Q and U maps that primarily contain the B -mode signal. At this stage, it becomes possible to train the neural network using the B -mode map derived from these polarization maps with the E -mode effectively removed. Under this assumption, DeepWiener is trained with the loss function J_B , equation (2.12), where σ^{*2} represents the variance map for the E -mode and B -mode maps, differing from the variance maps of the Q and U maps. Figure 4 shows the variance map for each pixel in the B -mode map and the corresponding histogram, computed from the difference of $B_{obs} - B_{sky}$. The intensity values of σ^{*2} differ from those of σ^2 , but the inhomogeneity pattern remains consistent.

Since the E-to-B leakage arises from the binary mask, we study the performance of the neural network in estimating the Wiener Filter of E and B considering two masks with different complexities and fractions of the sky. The left panel of Figure 5 shows a mask with only point sources of different sizes, while the right panel presents a mask with point sources and edges, covering a significant portion of the sky.

After the training, the models are used to estimate the power spectrum of maps with a different *true* angular power spectrum, obtained by slightly altering the cosmological parameters from their fiducial values. These maps, created using the *true* power spectrum, were not part of the training data, as the goal is to estimate the power spectrum of an unknown underlying signal. Each neural network used in this work was trained with the Apollo GPU nodes of the Institute for Advanced Studies, where each node contains 8 GPUs NVIDIA A100.

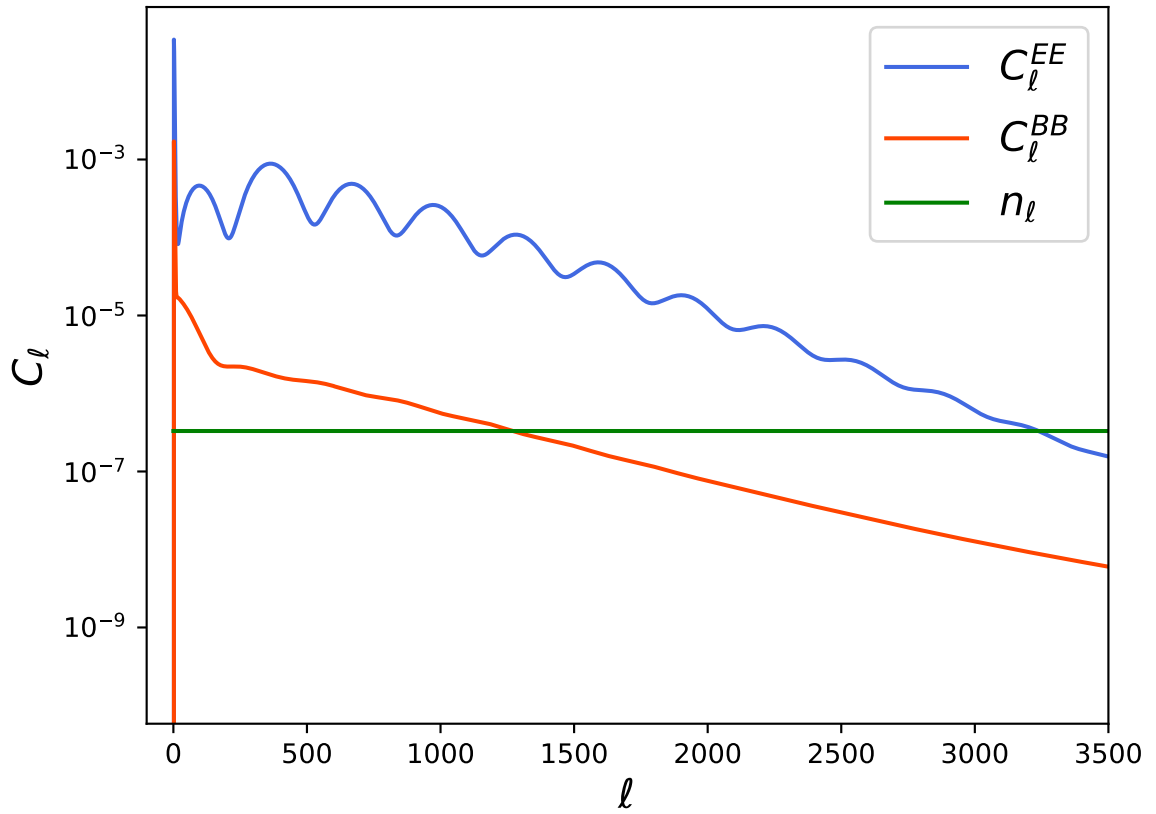


Figure 3. Power spectrum of the E-mode and B-mode signal and average noise level of the variance map extracted from Planck.

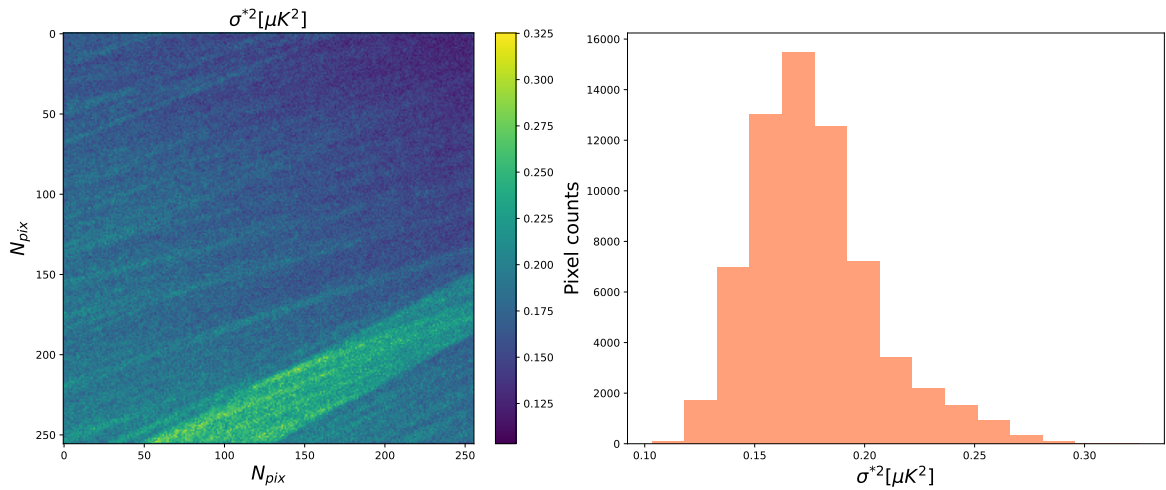


Figure 4. Left panel: Variance map for the B-mode map calculated from the difference $B_{obs} - B_{sky}$. Right panel: Histogram of the variance map for the B-mode map showing the distribution of pixel counts across different noise variances.

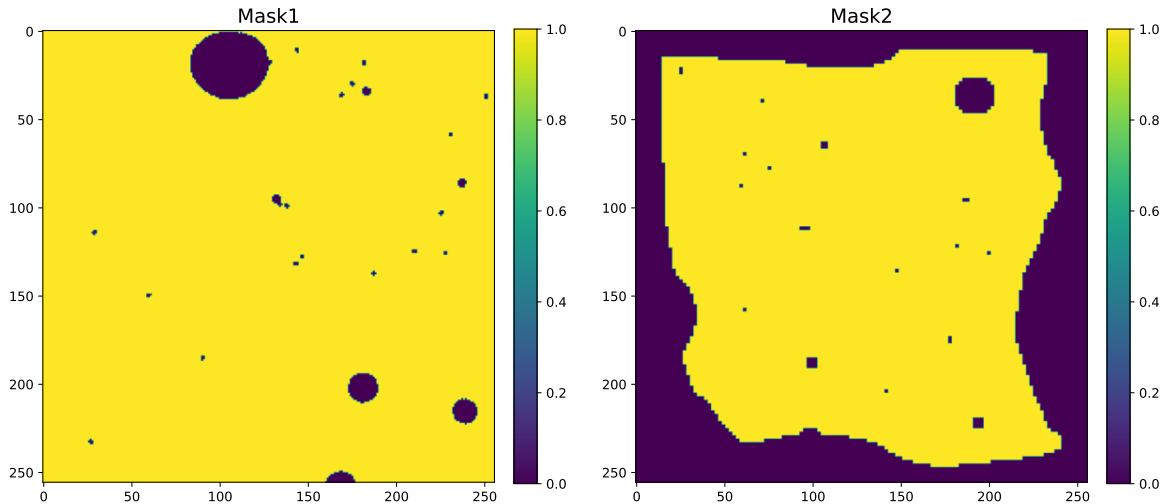


Figure 5. Left panel: mask with point sources of different sizes. Right panel: mask with tiny point sources and edges.

5 Results

5.1 Comparison with PCG results

We trained DeepWiener using TENSORFLOW 2 and PYTHON 3 on maps with 256×256 pixels experimenting with different hyperparameter values to ensure the minimization of the loss function. We obtained satisfactory results with a learning rate $lr = 3.36 \times 10^{-5}$ and a number of filters between 16 and 32 in each layer.

We constructed polarization datasets for training and validation, using the two masks shown in Figure 5, to evaluate the performance of the neural network under different mask complexities and sky coverage. In the initial training, we successfully reconstructed the E-mode WF but performed poorly on the B-mode due to the dominant E-mode contribution in the polarization maps. To address this, we retrained the network using a new dataset with the E-mode contribution from the first training removed. To mitigate the E-to-B leakage, we repeated this process multiple times, with each iteration removing the E-mode contribution obtained in the previous one. As anticipated, the more complex mask (Mask2) required more iterations (five), while the simpler mask (Mask1) required less iterations (four), using the loss function $J_{Q,U}$ defined in equation (2.6). Refer to Appendix C for detailed information about iterations results.

Figure 6 at the top compares a map of the E-mode signal, generated from the *fiducial* power spectrum, with the WF map computed with the PCG method and with the trained DeepWiener using the Mask1. On the bottom, it is the comparison of the B-mode signal with the corresponding WF reconstruction using the PCG method and the neural network. We can visually check that the outputs of DeepWiener and the procedure followed to address the E-to-B leakage on polarization maps are accurate to reconstruct the signal in unmasked pixels while reconstructing large-scale modes even in the masked region near the edges. These results were trained with the loss function $J_{Q,U}$ from equation (2.6).

Figure 7 presents the same comparison as in Figure 6, but with a more complex mask (Mask2) applied to the data. Qualitatively, it is evident that the E-mode reconstruction using PCG captures slightly more information near the edges compared to the E-mode results

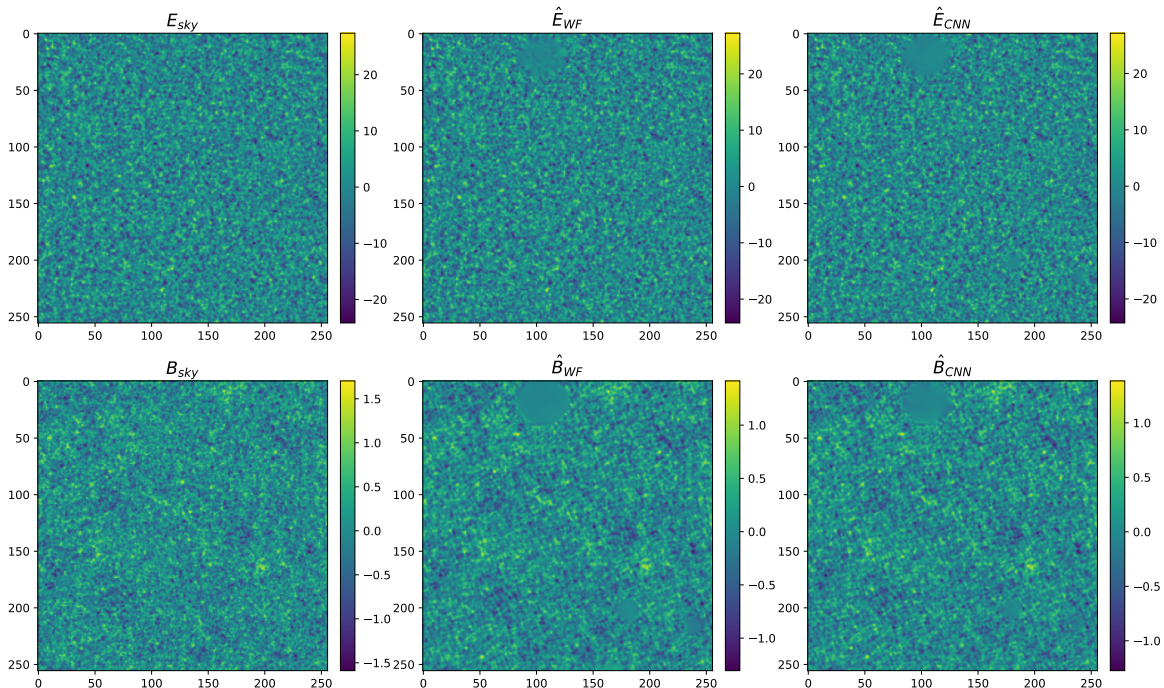


Figure 6. On the left panel it is presented an E-mode map signal and a B-mode map signal, simulated using the *fiducial* power spectrum. On the center it is presented the WF reconstruction with the PCG method for both modes with Mask1 applied, while on the right panel it is presented the reconstruction for both modes using DeepWiener and the loss function $J_{Q,U}$, equation (2.6).

obtained with DeepWiener. Additional training epochs may improve this, but the cross-correlation results indicate that the performance is already satisfactory, as it will be shown later. For the B-mode reconstruction, an additional iteration was required compared to Mask1 to achieve the results shown in the lower right panel, which visually are very similar to the PCG results.

The agreement in the WF simulated with DeepWiener and computed with PCG can be quantified using the cross-correlation coefficient r_ℓ as a function of the multipole ℓ . This coefficient measures how well the two methods align across different angular scales and is defined as:

$$r_\ell = \frac{\langle a_{CNN}(\ell) a_{WF}^*(\ell) \rangle}{\sqrt{\langle a_{CNN}(\ell) a_{CNN}^*(\ell) \rangle \langle a_{WF}(\ell) a_{WF}^*(\ell) \rangle}}, \quad (5.1)$$

where a_{CNN} refers to the discrete Fourier coefficients of either the E-mode or B-mode, depending on the output of the neural network. If the loss function $J_{Q,U}$ in equation (2.6) is used, a_{CNN} will be the E-mode or B-mode Fourier coefficients obtained from the Q and U maps filtered by the neural network. Alternatively, when the loss function J_B in equation (2.12) is used, a_{CNN} will represent the B-mode Fourier coefficients derived from the B-mode output map directly. Then, the cross-correlation coefficient r_ℓ is averaged over the test set (10 maps). This averaging provides a more robust measure of how well the two WF methods agree across different realizations.

The cross-correlation coefficient for the E-mode is presented in Figure 8, for data with Mask1 (left panel) and Mask2 (right panel) applied. With each iteration, the E-mode reconstruction improves as corrections are applied to the results from the previous iteration.

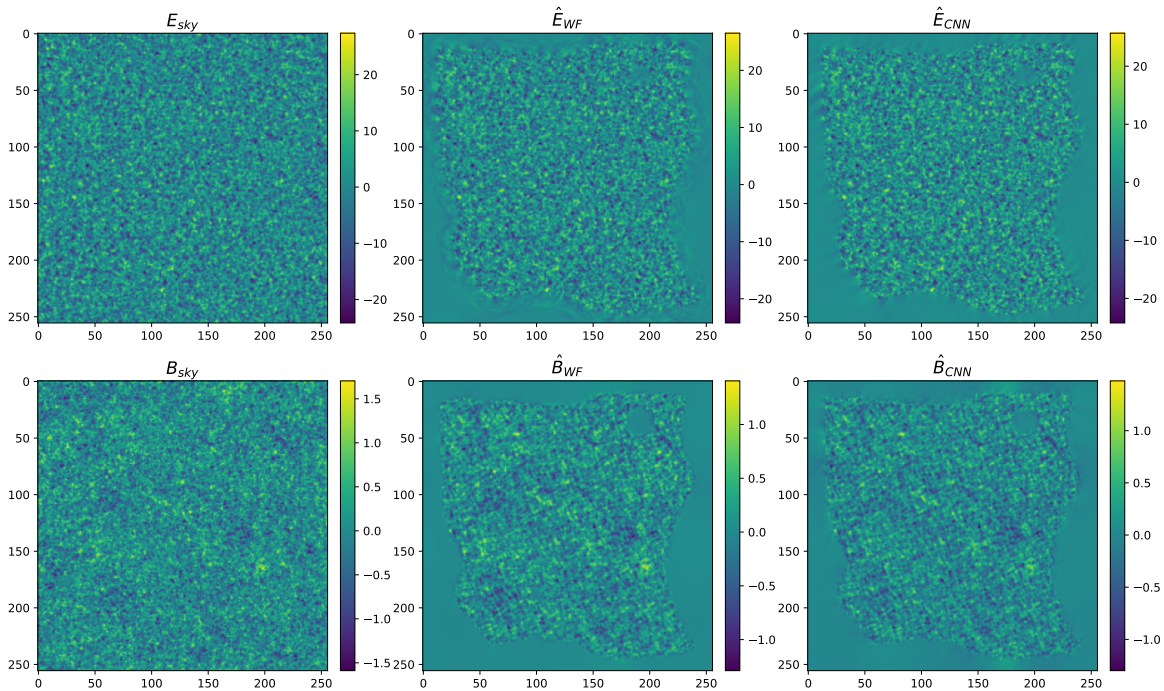


Figure 7. The left panel shows the E-mode and B-mode map signals, obtained from the *fiducial* power spectrum. The center panel presents the WF reconstruction using the PCG method for both fields with Mask2 applied. In the right panel, the reconstruction for both fields is shown using DeepWiener with the loss function $J_{Q,U}$ from equation (2.6).

Mask2 presents a more complex structure compared to Mask1, resulting in a more pronounced E-to-B leakage. Training additional epochs or performing more iterations is expected to be necessary to effectively mitigate leakage and achieve accurate signal reconstruction. More intermediate results are presented in Appendix C.

The E-mode reconstruction with the neural network shows a high correlation with the PCG method, which is expected since there is minimal noise contribution on the scales of interest, as shown in Figure 3. Figure 9 shows the cross-correlation coefficient for the B-mode, with Mask1 applied in the left panel and Mask2 in the right panel. In both cases, the noise becomes dominant at scales beyond $\ell \approx 1260$.

It is clear that the cross-correlation between the observed B-mode map (transformed from Q_{obs} and U_{obs} , with significant E-to-B leakage) and the WF computed using PCG highlights the improvement achieved by applying the DeepWiener models, especially on larger scales. Notably, the B-mode map reconstructed using DeepWiener trained with the loss function J_B (green curve) shows a higher correlation compared to the model trained with $J_{Q,U}$ (red curve). This indicates that the network performs better when a B-mode map is used as input instead of Q and U , leading to more accurate signal reconstruction. Besides, the number of iterations for the B-mode reconstruction using the loss function J_B is one less than using the loss function $J_{Q,U}$ (3 iterations for data with Mask1 and 4 iterations for data with Mask2).

In the next section, we will explore whether the performance of DeepWiener models with different loss functions and mask has any impact on the estimation of the power spectrum.

On Appendix D it is presented the computational time required to perform the WF using DeepWiener with several models, compared with the computational time using the

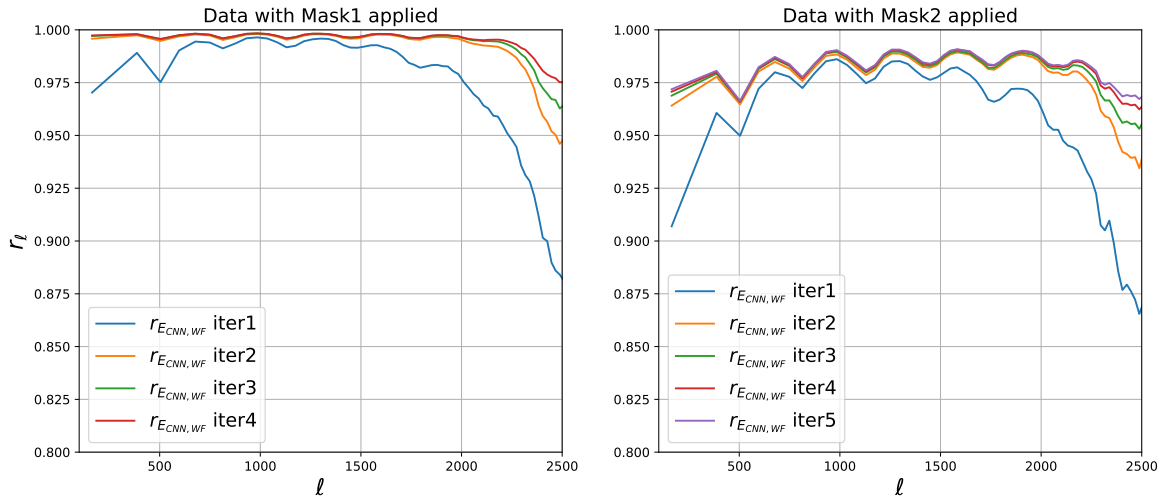


Figure 8. Cross-correlation coefficient for the E-mode map between the DeepWiener models and the WF with PCG, for each iteration. The left panel presents the results for data with Mask1 applied, while the right panel shows the results for Mask2.

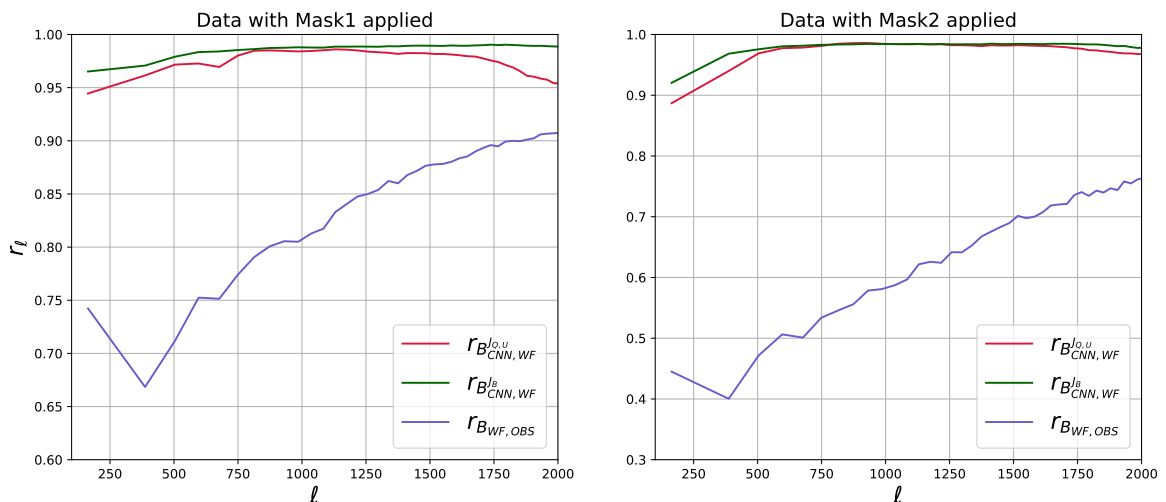


Figure 9. Cross correlation coefficient for the B-mode map between the DeepWiener models and the WF with PCG. The left panel presents the results for data with Mask1 applied, while the right panel shows the results for Mask2. In both cases, the final iteration result is shown where the E-mode contribution has been nearly removed. The red and green curves represent the cross-correlation using DeepWiener trained with the loss functions $J_{Q,U}$ (2.6) and J_B (2.12), respectively. Additionally, the cross-correlation coefficient between the observed B-mode map and the B-mode WF is also included for comparison.

PCG method.

5.2 Implementation of the power spectrum

For the estimation of the power spectrum, it is necessary to assess the noise bias and the Fisher matrix for both E-mode and B-mode, as presented in section 2. This evaluation takes place after the estimation of the underlying field \hat{s} , for which the selection of a *fiducial* angular

power spectrum is required. Then, we computed the noise bias and Fisher matrix through simulations of the *fiducial* power spectrum.

We started generating a Gaussian realization of the signal in Fourier space, for the E-mode and B-mode, denoted as \mathbf{s}_s^E and \mathbf{s}_s^B respectively:

$$\langle |\mathbf{s}_s^E|^2 \rangle = \mathbf{S}_{fid}^E \quad (5.2)$$

$$\langle |\mathbf{s}_s^B|^2 \rangle = \mathbf{S}_{fid}^B. \quad (5.3)$$

Then, we transformed properly to Q and U data since the received observations are not in the (E, B) basis. We generated random noise realizations using the variance map presented in Figure 2:

$$\mathbf{d}_{s+n}^Q = \mathbf{d}_s^Q + \mathbf{d}_n^Q \quad (5.4)$$

$$\mathbf{d}_{s+n}^U = \mathbf{d}_s^U + \mathbf{d}_n^U, \quad (5.5)$$

where we have considered that the noise realization is the same for Q and U , therefore $\mathbf{d}_n^Q = \mathbf{d}_n^U$.

We applied the DeepWiener models on these dataset and transformed to obtain $\hat{\mathbf{s}}_{s+n}^E$ and $\hat{\mathbf{s}}_{s+n}^B$. We have calculated the noise bias term for both modes, with the expression (2.23), averaged over several realizations, that enables to obtain an unbiased estimator of the power spectrum.

In the presence of a mask, the Fisher matrix accounts for the band-power mixing and can be interpreted as the response of the band-power ℓ to another band-power ℓ' . A small perturbation is introduced to a Gaussian realization of the *fiducial* power spectrum at a specific band-power ℓ' , leading to the following equation:

$$F_{\ell\ell'} \Delta\Theta_{\ell'} = E_{\ell}(\Theta_{fid}, \hat{\mathbf{s}}_{\ell', s+n}) - E_{\ell}(\Theta_{fid}, \hat{\mathbf{s}}_{s+n}), \quad (5.6)$$

that should be calculated for both E and B-modes.

After computing the noise bias and the Fisher matrix through simulations, averaged over several realizations, we estimated a new unknown *true* power spectrum, which was never part of the neural network training, using the expressions (2.25) and (2.26).

Figure 10 and 11 show the power spectrum estimation for both E-modes and B-modes, for a single map with Mask1 and Mask2 applied, and averaged over 100 maps. In the left panel, the E-mode case is presented, where there is no noise contribution at any scale, leading to an estimation that matches the *true* power spectrum. The middle and right panels display the B-mode case using models trained with $J_{Q,U}$ and J_B , respectively. On average, the B-mode estimation remains unbiased across all scales, although the estimation for individual maps becomes noisier at scales far beyond $\ell \approx 1260$, where the noise dominates. For now on, we will focus our analysis for the B-mode power estimation.

To compare the ability of the DeepWiener models, trained with different loss functions, to estimate the *true* B-mode power spectrum it is more clear to analyze the relative difference between the estimated B-mode power spectrum and the *true* power spectrum, as shown on Figure 12. The *fiducial* power spectrum serves as a starting point from which the unknown *true* power spectrum is estimated by applying a correction $\Delta\Theta$, that is computed through the outlined procedure. Consequently, the purple line represents the relative difference between the *true* and *fiducial* power spectra, reflecting a bias by construction.

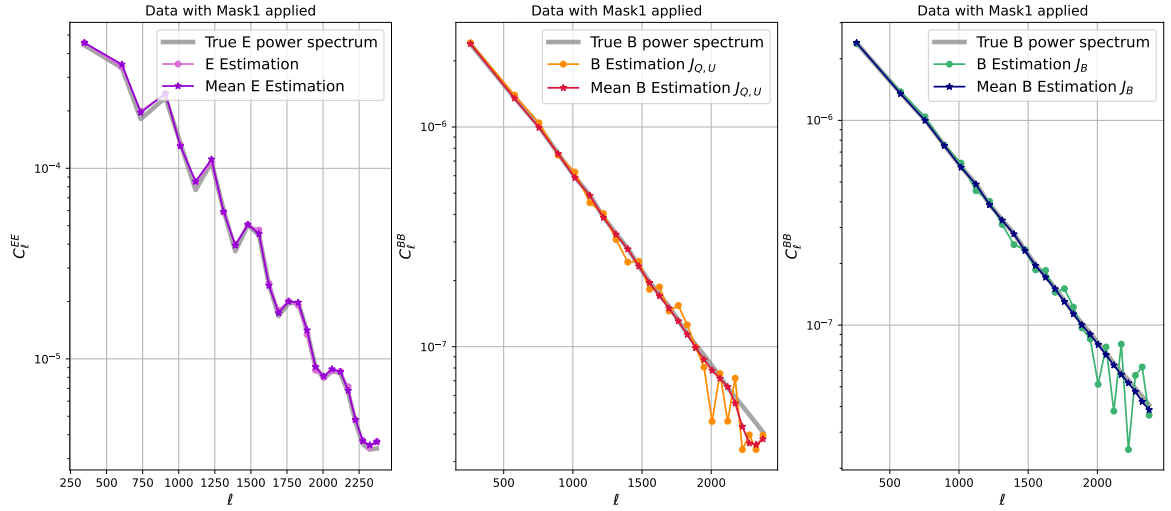


Figure 10. Left panel: estimation of the true E power spectrum for one map and the average estimation over 100 maps. Middle panel: estimation of the true B power spectrum for one map and the average over 100 maps, using DeepWiener models trained with $J_{Q,U}$ (2.6). Right panel: estimation of the true B power spectrum for one map and the average over 100 maps using DeepWiener models trained with J_B (2.12).

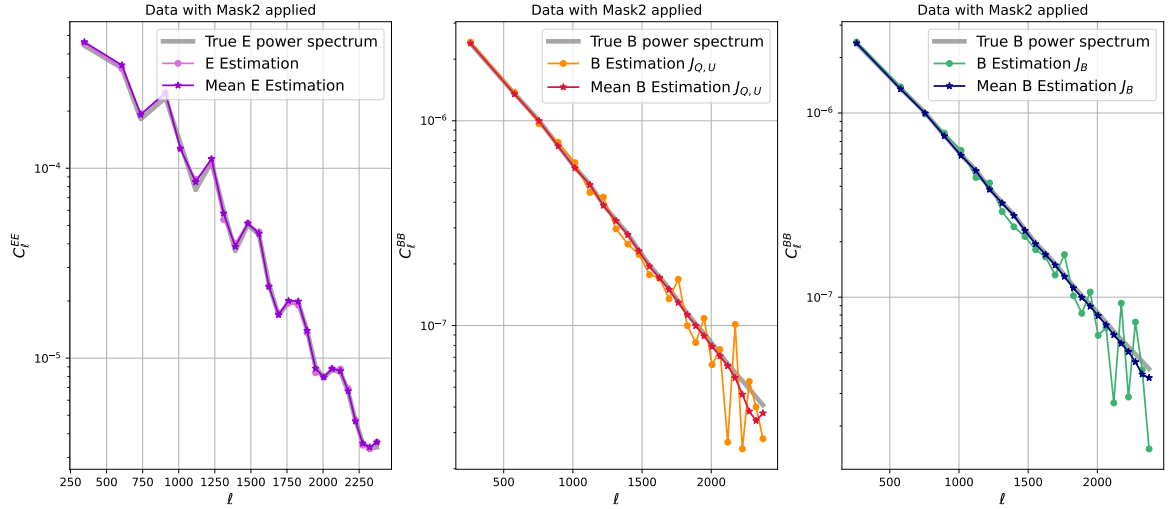


Figure 11. Left panel: estimation of the true E power spectrum for one map and the average estimation over 100 maps. Middle panel: estimation of the true B power spectrum for one map and the average over 100 maps, using DeepWiener models trained with $J_{Q,U}$ (2.6). Right panel: estimation of the true B power spectrum for one map and the average over 100 maps using DeepWiener models trained with J_B (2.12).

The left panels in Figure 12 display the relative difference between the estimated B-mode power spectrum and the *true* power spectrum for data with Mask1 applied, while the right panels show the same comparison for data with Mask2 applied. For all cases it is presented a single measurement and the average over 100 maps, along with the corresponding error bars. It is noticeable that the estimations are unbiased for both loss functions, as the values remain

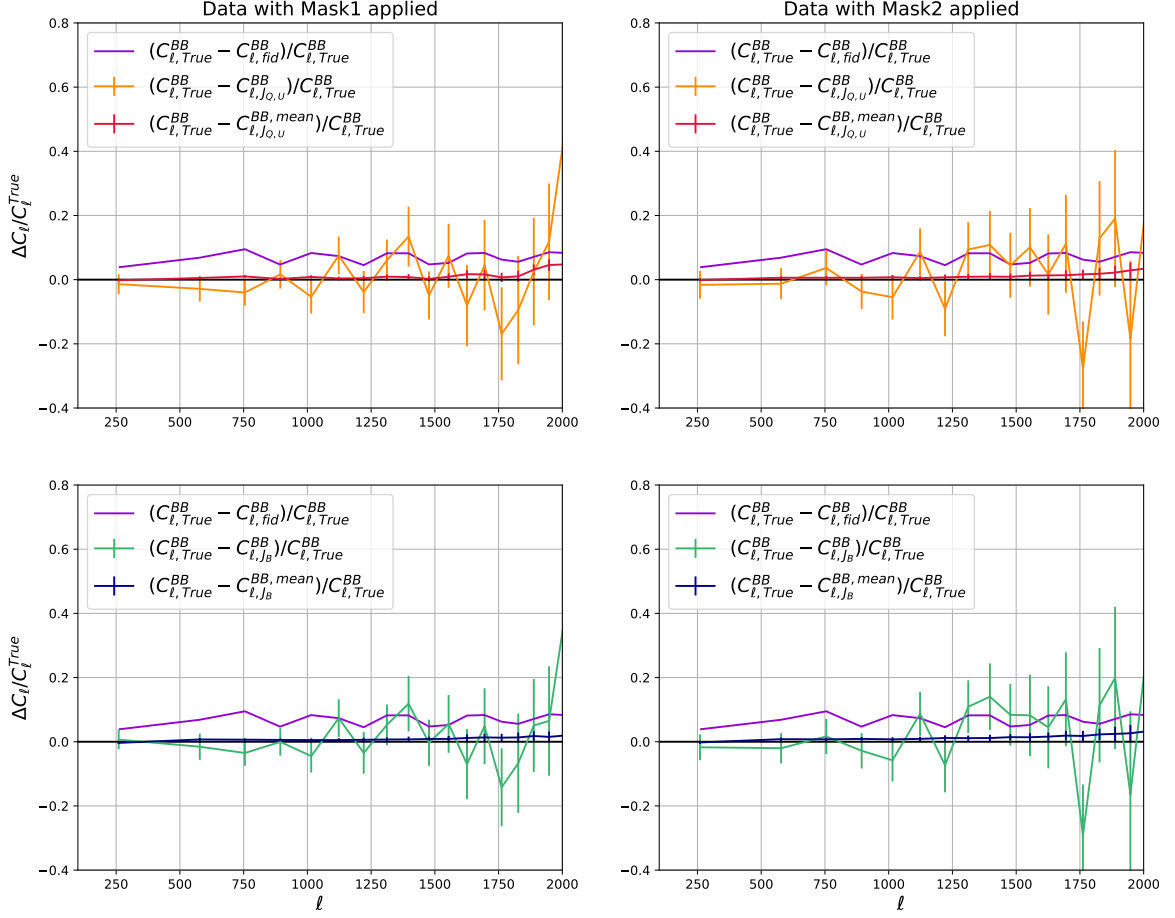


Figure 12. Relative difference between the true B power spectrum and the estimation of the power spectrum for models trained with $J_{Q,U}$ (2.6) (top panels) and J_B (2.12) (bottom panels), for data with Mask1 (left panels) and Mask2 (right panels) applied. It is presented, in each panel, the relative difference for the average estimation over 100 maps with the corresponding error bar, and the relative difference for the estimation of a single map.

centered around zero, specially for data with Mask1 applied. However, the error bars grow larger at scales beyond $\ell \approx 1260$, where the noise level becomes dominant compared to the signal, and the signal-to-noise ratio is quite smaller than one. This demonstrates that both loss functions are effective for estimating B_{WF} and its corresponding power spectrum.

It is worthwhile to compare the errors of the estimated power spectrum for a single map with the square root of the inverse of the Fisher matrix, F^{-1} . The inverse Fisher matrix can be interpreted as an estimate of the covariance matrix of the elements Θ_ℓ , assuming the modes are Gaussian distributed. Therefore, in Figure 13, the square root of the inverse Fisher matrix, calculated using equation (5.6), is presented for models trained with $J_{Q,U}$ (top panels) and J_B (bottom panels). The left panels show the comparison for data with Mask1 applied, while on the right panel it is presented for data with Mask2 applied. As expected, it closely matches the error in the estimation of the *true* power spectrum. A small difference can be observed since the Fisher matrix corresponds to the error of the *fiducial* power spectrum, while we are estimating an unknown power spectrum referred to as the *true* power spectrum.

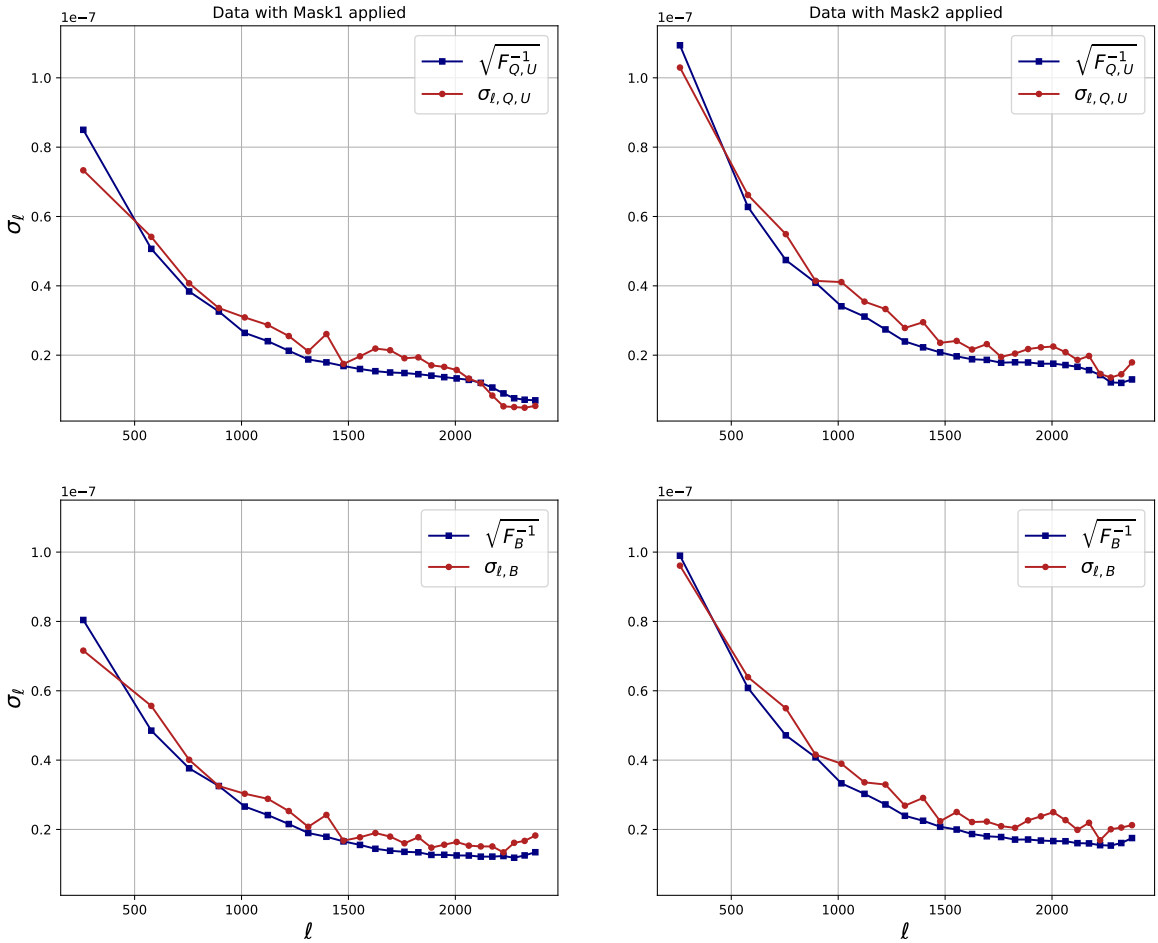


Figure 13. Square root of the diagonal part of the inverse Fisher matrix and the error of the estimation of the *true* power spectrum, for models trained with $J_{Q,U}$ (2.6) (top panels) and J_B (2.12) (bottom panels).

As it can be noticed from Figure 13, the errors on the left panels (data with Mask1) are smaller than the errors on the right panels (data with Mask2). Therefore, Figure 14 compares the power spectrum errors for data with Mask1 and Mask2 applied, where for the Mask1 case the uncertainties are rescaled by a factor equal to $\sqrt{f_{sky,mask1}/f_{sky,mask2}}$, f_{sky} representing the fraction of the sky that remains unmasked. The left panel shows the results using models trained with $J_{Q,U}$, while the right panel presents the results for models trained with J_B .

It is clear that the errors are larger when a more extensive mask is applied, as the fraction of the sky unmasked becomes smaller, making the power spectrum estimation more challenging. Then, the primary difference between the uncertainties, in each case, comes from the extension of the mask, as when one of them is rescaled by this effect, the curves closely match. In the next section, we aim to compare these errors with those obtained using the pseudo- C_ℓ approach.

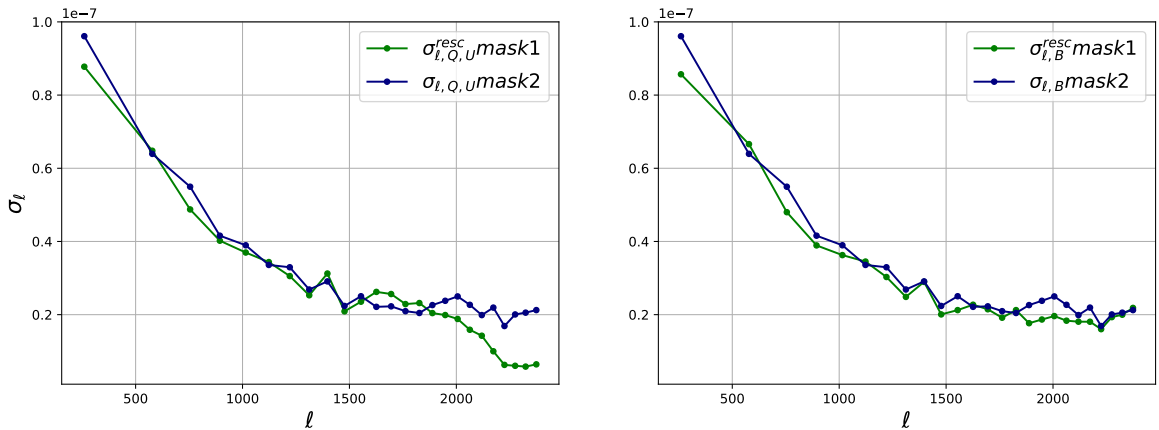


Figure 14. Left panel: error in the power spectrum estimation for models trained with $J_{Q,U}$ (2.6) and data with Mask1 (rescaled by a factor $\sqrt{f_{sky,mask1}/f_{sky,mask2}}$) and Mask2 applied. Right panel: error in the power spectrum estimation for models trained with J_B (2.12) and data with Mask1 (rescaled by a factor $\sqrt{f_{sky,mask1}/f_{sky,mask2}}$) and Mask2 applied.

5.3 Comparison with pseudo- C_ℓ estimator

The pseudo- C_ℓ algorithm estimates the power spectrum of spin-0 or spin-2 fields using the public library `NAMASTER`, introduced in [36]. This framework provides essential tools for power spectrum estimation of CMB maps, both on the sphere and in the flat-sky approximation, including contamination deprojection and E/B purification. The key difference compared to the optimal quadratic estimator, described in Section 2, lies in the substitution of the inverse covariance matrix (expressed as C^{-1} in equation (2.15)) with its diagonal, making it a more computationally efficient method. This approximation is optimal when the data have uncorrelated pixels, which is true if the noise is large and uncorrelated, or if the underlying power spectrum is close to white.

Given the widespread use of `NAMASTER`, we aim to compare the uncertainties computed with this library to the errors presented in the previous section, which applies the Wiener Filter through neural networks and calculates the optimal quadratic estimator via simulations. For that purposes, we estimate the *true* power spectrum given a dataset with inhomogeneous noise and the different masks applied, with the pseudo- C_ℓ method.

We follow the steps for the flat-sky approximation specified in [36]. The process begins with a naive estimator by calculating the auto-spectra of the observed map, which couples different multipoles ℓ due to the incomplete sky coverage. Consequently, it calculates an analytical expression for the mode-coupling matrix $M_{\ell\ell'}$, in order to correct this bias, based on [40]. Then, the pseudo- C_ℓ expression for spin-2 fields will be:

$$\begin{pmatrix} \tilde{C}_\ell^{EE} \\ \tilde{C}_\ell^{EB} \\ \tilde{C}_\ell^{BE} \\ \tilde{C}_\ell^{BB} \end{pmatrix} = (M_{\ell\ell'}^{22}) \begin{pmatrix} C_{\ell'}^{EE} \\ C_{\ell'}^{EB} \\ C_{\ell'}^{BE} \\ C_{\ell'}^{BB} \end{pmatrix}, \quad (5.7)$$

where the elements of $M_{\ell\ell'}^{22}$ depend of the mask harmonic coefficients w_{lm} by the auto-spectra of the mask (note that only for demonstration purposes we put the expression of the curved

sky case):

$$W_\ell = \sum_m w_{\ell m} w_{\ell m}^*. \quad (5.8)$$

In general, is not possible to invert $M_{\ell\ell}^{22}$ directly, therefore, the coupling matrix is binned into band-powers. The steps of the pseudo- C_ℓ calculation can be summarized in three stages: coupling the different multipoles by calculating the auto-spectra of the field, then binning into band-powers, and finally decoupling the band-powers with the inverted binned coupling matrix.

Since no Wiener Filter is applied in this method, we must estimate the noise bias by averaging the result of applying the pseudo- C_ℓ estimator to a large number of noise realizations (100 noise maps).

To mitigate E-to-B leakage, a purification method is available, which offers an analytical approximation for isolating the pure B-mode component. In the derivation of this expression, a differential operator, denoted as \mathbf{D}_s^B , is defined. Applying \mathbf{D}_s^B to a scalar field will give a pure B-mode. Then, the B-mode coefficients of a spin-2 field \mathbf{P} can be expressed as:

$$\tilde{B}_\ell \equiv \int d\hat{\mathbf{n}} w(\hat{\mathbf{n}}) ({}_s Y_\ell^B(\hat{\mathbf{n}}))^\dagger \mathbf{P} = \int d\hat{\mathbf{n}} w(\hat{\mathbf{n}}) (\mathbf{D}_s^B Y_\ell)^\dagger \mathbf{P}(\hat{\mathbf{n}}), \quad (5.9)$$

where w is the mask vector, that should be on the right of \mathbf{D}_s^B in order to consider $\mathbf{D}_s^B(wY_\ell)$ as a B-mode. Therefore, the pure B-mode component is:

$$B_\ell^p = \int d\hat{\mathbf{n}} (\mathbf{D}_s^B(wY_\ell))^\dagger \mathbf{P}(\hat{\mathbf{n}}). \quad (5.10)$$

Finally, expanding $\mathbf{D}_s^B(wY_\ell)$ results in an expression of B_ℓ^p that depends of the first and second derivatives of the mask vector, requiring apodization with a window function for accurate application. We refer to [36] for more details in the calculations.

For both masks, we applied a Gaussian window function to smooth the edges and enable the use of the purification method provided by the library. The estimator, using purification, will be unbiased if the mask is sufficiently smooth and differentiable. It is not always straightforward to do that, since a fraction of the signal is lost by the apodization of the mask.

We estimated the power spectrum for 100 maps and averaged the results. Figure 15 presents the relative difference between the *true* power spectrum and the average estimation obtained using the pseudo- C_ℓ calculation and our optimal quadratic estimator approach, along with their respective errors.

It is evident that the average pseudo- C_ℓ estimation is slightly biased, especially in the first bin, and more pronounced for data with Mask1 applied (left panel), which does not occur with our estimation approach. Additionally, our optimal quadratic estimator method did not require the application of an apodization function.

In order to establish the precision using both methods, we compared the error of the power spectrum estimation for a single measurement. Figure 16 presents the pseudo- C_ℓ error with E/B purification in the orange curve, which is noticeably larger in the first bin (where the primordial B-modes appear) compared to the power spectrum error obtained with our approach. The second bin also exhibits a larger error than ours, but for scales beyond $\ell \approx 750$, the errors become quite similar. Therefore, the purification method results in smaller errors for scales beyond $\ell \approx 750$, but incurs inaccuracies in the largest scales.

In addition, the green curves show the measurement errors without the purification method applied, which are larger than our uncertainties across all scales. It is clear that the

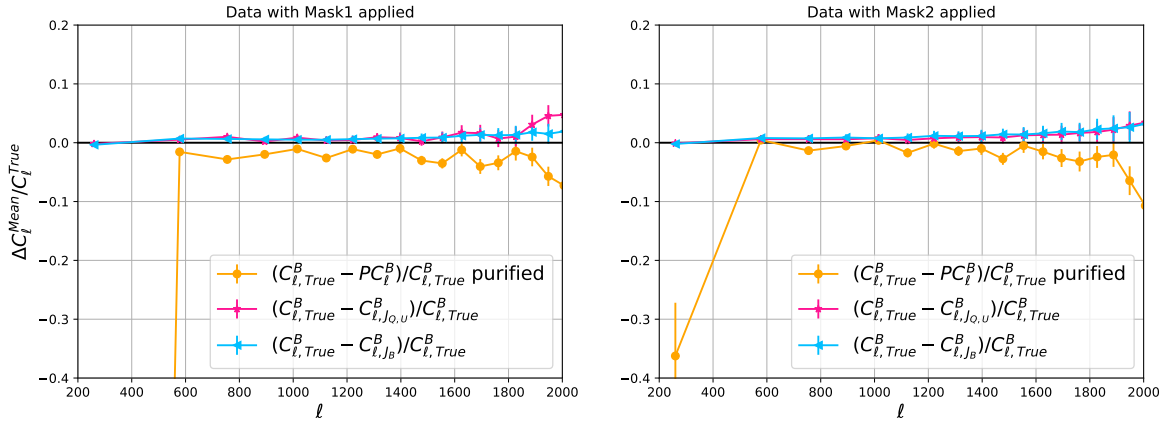


Figure 15. On the left panel it is presented the relative difference between the *true* power spectrum and the average power spectrum estimation over 100 maps for data with Mask1 applied, while on the right panel it is presented the same comparison but for data with Mask2 applied.

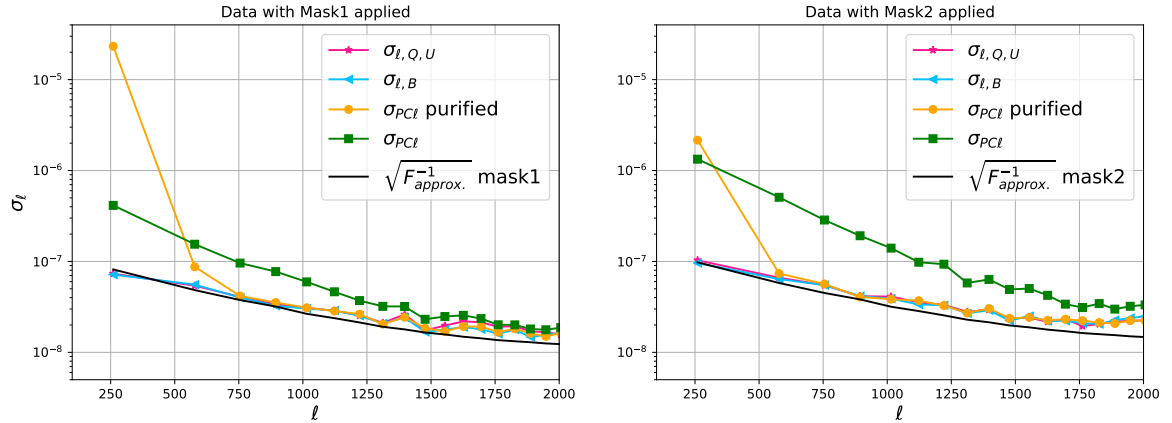


Figure 16. Comparison between the pseudo- C_ℓ estimation error (with and without purification) and the estimated errors following our approach. On the left panel for data with Mask1 applied, and on the right panel for data with Mask2 applied. Additionally, it is presented an approximated expression of the Fisher matrix (black curves).

E/B purification reduces errors in the pseudo- C_ℓ estimation for scales beyond $\ell \approx 750$, but it performs worse at the largest scales, likely due to apodization.

We have used, as reference, the approximation of the Fisher matrix when homogeneous noise is applied (considering the average of the inhomogeneous noise), $F_{approx} = f_{sky} F_{\ell\ell'}$, where f_{sky} is the fraction of the sky unmasked (different for both masks), and $F_{\ell\ell'}$ is the cosmic variance error for maps without mask applied (without mode coupling).

Finally, as expected, the errors obtained using a quadratic estimator approach (with an approximated WF through neural networks) are smaller than the pseudo- C_ℓ errors, and the average estimation is slightly more accurate than the pseudo- C_ℓ estimation. Using DeepWiener for the WF simulation allows the efficient application of the optimal quadratic estimator for the power spectrum computation given a set of noisy maps.

6 Conclusion

In this paper, we present a neural network model called DeepWiener, designed to simulate the Wiener Filter for application to CMB polarization maps with inhomogeneous noise applied. Using the trained models, we efficiently compute the E-mode and B-mode power spectra, implementing a simulation-based optimal quadratic estimator within a reasonable computation time.

The neural network’s performance is highly dependent on careful hyperparameter selection; however, achieving optimal reconstruction for both E-modes and B-modes is challenging due to E-to-B leakage. Usually, E-modes are well-reconstructed in the initial training, as they dominate the Q and U maps. To address this, we propose an iterative approach: in each iteration, a new dataset is generated with the E-mode reconstruction from the previous iteration removed, allowing the network to capture the B-modes in the signal.

We employed the loss function $J_{Q,U}$ in equation (2.6) when the network’s inputs are the Q and U maps, which is the same expression as the χ^2 function that must be minimized to obtain the WF solution. When the dataset predominantly contains B-modes, with most E-mode contribution removed, we also apply the proposed loss function J_B in equation (2.12), similar to the case of a scalar field like temperature. Here, the neural network receives the observed B-mode as input and directly outputs the WF of the B-mode map.

In Figure 8, we demonstrate that the reconstruction of the E-mode improves with each iteration using the loss function $J_{Q,U}$, as it also recovers residual E-mode contributions in the Q and U maps. Figure 9 shows the B-mode reconstruction in the final iteration, with a comparison of both loss functions $J_{Q,U}$ and J_B . It is evident that the B-mode WF obtained using the loss function J_B aligns more closely with the WF produced by the PCG method, than the reconstruction with the loss function $J_{Q,U}$. This likely occurs because the neural network trained with Q and U maps attempts to recover some residual E-modes, while the network receiving the observed B-mode map focuses exclusively on that component. The use of the loss function J_B is appropriate once the E-to-B leakage is significantly reduced; otherwise, the observed B-map would be heavily contaminated by E-mode contributions.

The cases considered include CMB polarization maps with inhomogeneous noise applied, and two masks, covering different fraction of the sky. Given that the primary challenge in this work is the E-to-B leakage, we demonstrate the neural network’s capacity to simulate the WF across datasets with different mask complexities. For a dataset with Mask1 applied (see Figure 5), 4 iterations were necessary, whereas 5 iterations were required for Mask2, using loss function $J_{Q,U}$. When using loss function J_B , the number of required iterations decreased to 3 for Mask1 and 4 for Mask2.

Additionally, we present the power spectrum estimation of an unknown signal for the E-modes and B-modes using a simulation-based optimal quadratic estimator. This approach was feasible because predictions made with the trained models are significantly faster than computing the WF via the PCG method, even though each map requires 4 or 5 model applications. In Appendix D we calculate the computation time for DeepWiener models compared with PCG. Calculating the noise bias required applying the WF to 100 maps, and the Fisher matrix calculation to 2000 maps, a scale that would be impractical to achieve with the traditional Conjugate Gradient method within a reasonable time.

To verify that the procedure was performed correctly, Figure 13 shows that the errors in the power spectrum estimation closely match the square root of the inverse of the Fisher matrix, which, by definition, represent the covariance matrix of the power spectrum.

We remark that achieving satisfactory convergence for the B-mode reconstruction is more challenging for the dataset with Mask2 applied compared to Mask1. Furthermore, Figure 14 clearly shows that the power spectrum errors are higher for the dataset with Mask2 due to the smaller unmasked sky fraction.

Finally, we show on Figures 15 and 16 that the estimation with our procedure is more accurate than the pseudo- C_ℓ method, as our errors are smaller in the first bins and the average estimation is unbiased. It is expected since the pseudo- C_ℓ method does not solve the optimal quadratic estimator.

In future work, we aim to apply these methods on a real-world CMB experiments, such as the Q & U Bolometric Interferometer for Cosmology, QUBIC [14], with more complex noise properties. Besides, we plan to explore the improvements in the neural network architecture by incorporating more complex Deep Learning models currently used in Computer Vision [41]. Another possible approach would be to implement a new neural network architecture that directly estimates the power spectrum from a set of observed maps, using a quadratic form in the data, similar to the optimal quadratic estimator.

A Conjugate gradient algorithm

The conjugate gradient (CG) is an iterative numerical method that solve linear system equations of the form:

$$\mathbf{A}\mathbf{x} = \mathbf{b}, \quad (\text{A.1})$$

where the known $n \times n$ matrix \mathbf{A} is real, symmetric ($\mathbf{A}^T = \mathbf{A}$) and positive definite ($\mathbf{x}^T \mathbf{A} \mathbf{x} > 0$, for all non-zero \mathbf{x}).

In order to find the WF estimator, the system that needs to be solved is:

$$(\mathbf{S}^{-1} + \mathbf{R}^\dagger \mathbf{N}^{-1} \mathbf{R}) \mathbf{x} = \mathbf{R}^\dagger \mathbf{N}^{-1} \mathbf{d}, \quad (\text{A.2})$$

where \mathbf{d} represents the Q and U components in configuration space, \mathbf{x} corresponds to the E and B components in Fourier space, and the response matrix \mathbf{R} acts as an operator that transforms from Fourier space to configuration space and applies the rotation from Q and U to E and B , as detailed in Appendix B. The goal is to invert the problem and find a solution of the unknown vector \mathbf{x} . Compared to equation (A.1), in this case, $\mathbf{b} = \mathbf{R}^\dagger \mathbf{N}^{-1} \mathbf{d}$ and $\mathbf{A} = (\mathbf{S}^{-1} + \mathbf{R}^\dagger \mathbf{N}^{-1} \mathbf{R})$.

The general idea of the algorithm is to start from an initial guess for \mathbf{x} , $\mathbf{x}_0 = 0$, which is iteratively updated based on a metric indicating its proximity to the solution \mathbf{x}_* . The solution has to be the unique minimizer of the quadratic function:

$$f(\mathbf{x}) = \frac{1}{2} \mathbf{x}^T \mathbf{A} \mathbf{x} - \mathbf{x}^T \mathbf{b}, \quad \mathbf{x} \in R^n. \quad (\text{A.3})$$

This function is minimized when its gradient is equal to zero:

$$\nabla f = \mathbf{A}\mathbf{x} - \mathbf{b}, \quad (\text{A.4})$$

which is equal to equation (A.1). The minimization proceeds by generating a sequence of search directions \mathbf{p}_k , and updated solutions, \mathbf{x}_k . In each iteration, a quantity α_k is determined that minimizes $f(\mathbf{x}_k + \alpha_k \mathbf{p}_k)$, and \mathbf{x}_{k+1} is then set to $\mathbf{x}_k + \alpha_k \mathbf{p}_k$.

The algorithm begins by defining the residual $\mathbf{r} = \mathbf{b} - \mathbf{A}\mathbf{x}$. If the residual is sufficiently small for the initial guess \mathbf{x}_0 , then \mathbf{x}_0 is returned as the result. Otherwise, set $\mathbf{p}_0 = \mathbf{r}_0$ and enter the iteration loop, which proceeds as follows:

$$\alpha_k = \frac{\mathbf{r}_k^T \mathbf{r}_k}{\mathbf{p}_k^T \mathbf{A} \mathbf{p}_k} \quad (\text{A.5})$$

$$\mathbf{x}_{k+1} = \mathbf{x}_k + \alpha_k \mathbf{p}_k \quad (\text{A.6})$$

$$\mathbf{r}_{k+1} = \mathbf{r}_k - \alpha_k \mathbf{A} \mathbf{p}_k \quad (\text{A.7})$$

$$\beta_k = \frac{\mathbf{r}_{k+1}^T \mathbf{r}_{k+1}}{\mathbf{r}_k^T \mathbf{r}_k} \quad (\text{A.8})$$

$$\mathbf{p}_{k+1} = \mathbf{r}_{k+1} + \beta_k \mathbf{p}_k, \quad (\text{A.9})$$

The loop continues until the residual \mathbf{r}_{k+1} is sufficiently small, at which point \mathbf{x}_{k+1} is returned as the result. For a more detailed explanation of the procedure, refer to [21].

The matrix $(\mathbf{S}^{-1} + \mathbf{R}^\dagger \mathbf{N}^{-1} \mathbf{R})$ can become ill-conditioned when its condition number is large, which can significantly slow down the method. This poor conditioning is typically caused by \mathbf{S}^{-1} . To improve the conditioning, it is necessary to define a preconditioner, which is a non-singular matrix that transforms the problem into an equivalent one with better conditioning. A simple choice for the preconditioner is \mathbf{S}^{-1} [42].

Following the described method, we developed our own code to solve the linear system, based on the QUICKLENS package², which is included in the DeepWiener repository.

B Partial sky polarization

The CMB radiation is characterized by the Stokes parameters I , Q , and U . The parameter I denotes the intensity of the radiation at an observed position \hat{n} , while Q and U describe the linear polarization in Cartesian coordinates, rotated by 45° , respectively. The CMB temperature anisotropies are measured as fluctuations in intensity, which correspond to a spin-0 (scalar) field. In contrast, the linearly polarized components Q and U are coordinate-dependent quantities that transform under coordinate rotations in the plane perpendicular to direction \hat{n} . Then, the polarization can be expressed using two complex spin-2 fields:

$$P_\pm = Q \pm iU, \quad (\text{B.1})$$

which transform as:

$$P_\pm \mapsto P_\pm e^{\mp 2i\phi}, \quad (\text{B.2})$$

under a right-handed rotation by an angle ϕ .

These fields can be decomposed using the spin-weighted spherical harmonics ${}_s Y_{\ell m}$ with spin weights $s = \pm 2$:

$$P_\pm(\hat{n}) = \sum_{\ell m} a_{\pm 2, \ell m} Y_{\pm 2, \ell m}(\hat{n}), \quad (\text{B.3})$$

where \hat{n} is the observational position vector and $a_{\pm 2, \ell m}$ are the expansion coefficients.

It is convenient to express the polarization in terms of the scalar E-mode and pseudo-scalar B-mode, to define the power spectrum using rotationally invariant quantities [1, 43],

²<https://github.com/dhanson/quicklens>

where the harmonic coefficients are:

$$a_{E,\ell m} = -\frac{1}{2}(a_{2,\ell m} + a_{-2,\ell m}), \quad (\text{B.4})$$

$$a_{B,\ell m} = \frac{i}{2}(a_{2,\ell m} - a_{-2,\ell m}). \quad (\text{B.5})$$

These combinations behave differently under parity transformation:

$$a_{E,\ell m} \mapsto (-1)^\ell a_{E,\ell m}, \quad (\text{B.6})$$

$$a_{B,\ell m} \mapsto (-1)^{\ell+1} a_{B,\ell m} \quad (\text{B.7})$$

In the flat-sky approximation, instead of spherical decomposition, a plane wave expansion is used. For example, for temperature anisotropies:

$$\sum_{\ell m} a_{T,\ell m} Y_{\ell m}(\boldsymbol{\theta}) \rightarrow \int d^2\boldsymbol{l} T(\boldsymbol{l}) e^{i\boldsymbol{l}\cdot\boldsymbol{\theta}}, \quad (\text{B.8})$$

where, instead of the multipoles ℓ, m , the analysis is performed in terms of \boldsymbol{l} , a vector in the 2D Fourier plane. Then, the definitions of the E and B-modes are modified accordingly [44]:

$$a_{E,\ell m} \rightarrow E(\boldsymbol{l}) \equiv Q(\boldsymbol{l})\cos(2\phi_l) + U(\boldsymbol{l})\sin(2\phi_l), \quad (\text{B.9})$$

$$a_{B,\ell m} \rightarrow B(\boldsymbol{l}) \equiv -Q(\boldsymbol{l})\sin(2\phi_l) + U(\boldsymbol{l})\cos(2\phi_l), \quad (\text{B.10})$$

where ϕ_l is the angle between \boldsymbol{l} and the positive l_x axis.

C Neural network iterations

As referenced throughout the paper, especially in the results section 5, we performed several training stages, specified as iterations, where the E-mode contribution from the previous iteration is progressively removed. This iterative approach is needed because the CMB polarization is predominantly composed of E-modes, with amplitudes at least two orders of magnitude larger than B-modes. Nevertheless, although the primordial B-modes have a very faint signal, developing new techniques to detect them is crucial, as they serve as evidence of the inflationary epoch.

The observed Q_{obs} and U_{obs} polarization maps, that an instrument could measure, contain contributions from both the E-modes and B-modes. Since the E-modes represent the dominant signal in these maps, the first training of DeepWiener extract the polarization information present on these modes. While the reconstructed E-mode signal, E_{NN} , obtained by the neural network is generally accurate, the main objective is to recover the B-mode signal, B_{NN} , which is largely obscured by the E-mode contribution.

In each iteration, a new dataset is generated by removing the E_{NN} contribution obtained from the previous iteration, enabling the network to focus on B-modes, which are the remaining contribution in the polarization maps. The outputs of DeepWiener, depending of the inputs provided, yield both a correction to the E-mode reconstruction from the previous iteration and the extracted B-mode contribution for the current iteration.

Figure 17 presents the WF of the B-modes for each iteration, obtained with DeepWiener, for the dataset with Mask1 applied. Each iteration shows an improvement in the B-mode reconstruction. The first iteration fails to recover almost any B-mode signal, while the final iteration closely resembles the expected result from the PCG algorithm.

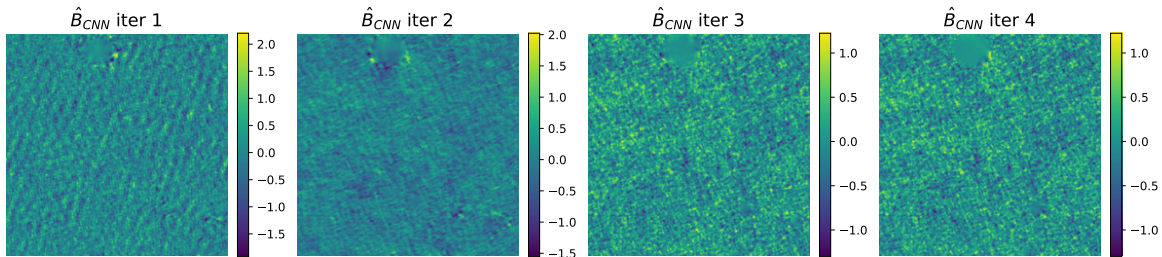


Figure 17. B-mode reconstruction in each DeepWiener iteration, for a dataset with Mask1 applied and using the loss function $J_{Q,U}$, equation (2.6).

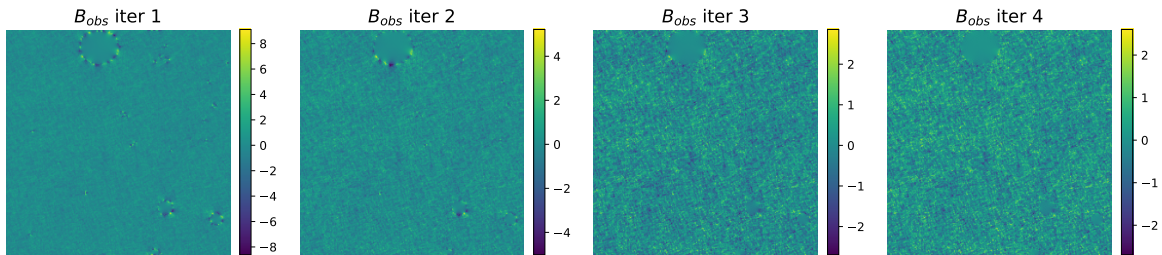


Figure 18. Observed B-mode transformed from Q_{obs}^i and U_{obs}^i at each iteration, for a dataset with Mask1 applied.

From Figure 18 it is evident that the observed B-mode map, transformed from Q_{obs}^i and U_{obs}^i , progressively reduces the E-to-B leakage at the edges of Mask1. This improvement occurs as the E-mode contribution is incrementally removed with each iteration. The observed B-mode map of the third iteration is used as input of DeepWiener when it is trained with the loss function J_B , equation (2.12).

D Computation time

In previous work [28, 45], we investigated the computational efficiency of applying the WF using neural network models compared to the PCG method. We tested various cases involving temperature maps with homogeneous noise, considering different noise levels and number of pixels. The results demonstrated that once the neural network is trained, performing predictions on a test set is significantly faster and more computationally efficient than calculating the WF through the PCG algorithm.

A neural network is trained only once, and the resulting trained model can then be applied to any map with the same characteristics as those used during training. Because the predictions with the trained models are extremely fast, this approach allows the WF to be applied to a large number of maps efficiently. Conversely, implementing the WF with the PCG method requires performing iterative inversion for each map. This makes the PCG approach computationally inefficient and even prohibitive when working with large maps.

Having a faster method to approximately perform the WF, enable to calculate the noise bias term and fisher matrix through simulations (100 maps for the noise bias and 2000 maps for the fisher matrix).

In this work, when new Q_{obs} and U_{obs} maps are received, it is necessary to apply a series of trained models depending on the mask used and the loss function implemented.

For instance, using the loss function $J_{Q,U}$, 5 models were used for Mask2 and 4 models for Mask1. When the loss function J_B is used, 4 models were necessary to achieve a good performance considering the Mask2, and 3 models for the Mask1. It is important to note that the prediction time will depend on the number of weights of the model, which is the same for all of them in any Mask case. Then the computation time will only increase if more models are implemented, independently of the Mask and loss function used.

Then, we calculate the computational time to apply those models on a test set of 100 maps and compare it with the computational time with the PCG algorithm. The last method will depend on the complexity of the Mask used and, therefore will be different for Mask1 and Mask2.

These results are presented in Table 1, in seconds and minutes, where it can be noticed that the prediction time using several models is faster (a factor order of 10) than the PCG method. Note that these calculations were performed on a CPU.

Although this comparison in computational time is based on 100 maps, the Fisher matrix estimation requires applying the WF to 2000 maps or more, where the PCG method could take several days to complete.

	CNN			PCG	
Time	3 models	4 models	5 models	Mask1	Mask2
[sec]	462.85	628.55	792.19	6776.4	9756.2
[min]	7.71	10.4	13.20	112.94	162.60

Table 1. Computing time, in seconds and minutes, required to estimate the WF on 100 maps. Left table: using CNN and different number of models depending of the case. Right table: using PCG and different Mask applied to the data.

Acknowledgements

M.B.C. acknowledges a doctoral fellowship by CONICET. C.G.S. and M.B.C. acknowledge funding from CONICET (PIP-2876), and Universidad Nacional de La Plata (G11-175), Argentina. M.Z. is supported by NSF 2209991 and NSF-BSF 2207583. The training of the neural networks and the simulations used here were performed at the SNS Supercomputing Center, at the Institute for Advanced Studies, in Princeton.

References

- [1] M. Zaldarriaga and U. Seljak, *All-sky analysis of polarization in the microwave background*, *Phys. Rev. D* **55** (1997) 1830 [[astro-ph/9609170](#)].
- [2] G. Hinshaw, D. Larson, E. Komatsu, D.N. Spergel, C.L. Bennett, J. Dunkley et al., *Nine-year Wilkinson Microwave Anisotropy Probe (WMAP) Observations: Cosmological Parameter Results*, *ApJS* **208** (2013) 19 [[1212.5226](#)].
- [3] C.L. Bennett, D. Larson, J.L. Weiland, N. Jarosik, G. Hinshaw, N. Odegard et al., *Nine-year Wilkinson Microwave Anisotropy Probe (WMAP) Observations: Final Maps and Results*, *ApJS* **208** (2013) 20 [[1212.5225](#)].
- [4] Planck Collaboration, N. Aghanim, Y. Akrami, F. Arroja, M. Ashdown, J. Aumont et al., *Planck 2018 results. I. Overview and the cosmological legacy of Planck*, *A&A* **641** (2020) A1 [[1807.06205](#)].

- [5] Planck Collaboration, N. Aghanim, Y. Akrami, M. Ashdown, J. Aumont, C. Baccigalupi et al., *Planck 2018 results. V. CMB power spectra and likelihoods*, *A&A* **641** (2020) A5 [[1907.12875](#)].
- [6] S. Aiola, E. Calabrese, L. Maurin, S. Naess, B.L. Schmitt, M.H. Abitbol et al., *The Atacama Cosmology Telescope: DR4 maps and cosmological parameters*, *J. Cosmology Astropart. Phys.* **2020** (2020) 047 [[2007.07288](#)].
- [7] S.K. Choi, M. Hasselfield, S.-P.P. Ho, B. Koopman, M. Lungu, M.H. Abitbol et al., *The Atacama Cosmology Telescope: a measurement of the Cosmic Microwave Background power spectra at 98 and 150 GHz*, *J. Cosmology Astropart. Phys.* **2020** (2020) 045 [[2007.07289](#)].
- [8] J.W. Henning, J.T. Sayre, C.L. Reichardt, P.A.R. Ade, A.J. Anderson, J.E. Austermann et al., *Measurements of the Temperature and E-mode Polarization of the CMB from 500 Square Degrees of SPTpol Data*, *ApJ* **852** (2018) 97 [[1707.09353](#)].
- [9] M. Hazumi, P.A.R. Ade, A. Adler, E. Allys, K. Arnold, D. Auguste et al., *LiteBIRD satellite: JAXA's new strategic L-class mission for all-sky surveys of cosmic microwave background polarization*, in *Space Telescopes and Instrumentation 2020: Optical, Infrared, and Millimeter Wave*, M. Lystrup and M.D. Perrin, eds., vol. 11443 of *Society of Photo-Optical Instrumentation Engineers (SPIE) Conference Series*, p. 114432F, Dec., 2020, DOI [[2101.12449](#)].
- [10] S. Hanany, M. Alvarez, E. Artis, P. Ashton, J. Aumont, R. Aurlien et al., *PICO: Probe of Inflation and Cosmic Origins*, *arXiv e-prints* (2019) [arXiv:1902.10541](#) [[1902.10541](#)].
- [11] B.A. Benson, P.A.R. Ade, Z. Ahmed, S.W. Allen, K. Arnold, J.E. Austermann et al., *SPT-3G: a next-generation cosmic microwave background polarization experiment on the South Pole telescope*, in *Millimeter, Submillimeter, and Far-Infrared Detectors and Instrumentation for Astronomy VII*, W.S. Holland and J. Zmuidzinas, eds., vol. 9153 of *Society of Photo-Optical Instrumentation Engineers (SPIE) Conference Series*, p. 91531P, July, 2014, DOI [[1407.2973](#)].
- [12] P. Ade, J. Aguirre, Z. Ahmed, S. Aiola, A. Ali, D. Alonso et al., *The Simons Observatory: science goals and forecasts*, *J. Cosmology Astropart. Phys.* **2019** (2019) 056 [[1808.07445](#)].
- [13] K. Abazajian, G. Addison, P. Adshead, Z. Ahmed, S.W. Allen, D. Alonso et al., *CMB-S4 Science Case, Reference Design, and Project Plan*, *arXiv e-prints* (2019) [arXiv:1907.04473](#) [[1907.04473](#)].
- [14] J.C. Hamilton, L. Mousset, E.S. Battistelli, P. de Bernardis, M.A. Bigot-Sazy, P. Chanial et al., *QUBIC I: Overview and science program*, *J. Cosmology Astropart. Phys.* **2022** (2022) 034 [[2011.02213](#)].
- [15] L. Mousset, M.M. Gamboa Lerena, E.S. Battistelli, P. de Bernardis, P. Chanial, G. D'Alessandro et al., *QUBIC II: Spectral polarimetry with bolometric interferometry*, *J. Cosmology Astropart. Phys.* **2022** (2022) 035 [[2010.15119](#)].
- [16] A. Mennella, P. Ade, G. Amico, D. Auguste, J. Aumont, S. Banfi et al., *QUBIC: Exploring the primordial Universe with the Qamp;U Bolometric Interferometer*, *arXiv e-prints* (2018) [arXiv:1812.00785](#) [[1812.00785](#)].
- [17] M. Tegmark, *How to measure CMB power spectra without losing information*, *Phys. Rev. D* **55** (1997) 5895 [[astro-ph/9611174](#)].
- [18] N. Wiener, *Extrapolation, interpolation, and smoothing of stationary time series. Vol. 2*, MIT press, Cambridge, MA (1949).
- [19] S. Zaroubi, Y. Hoffman, K.B. Fisher and O. Lahav, *Wiener Reconstruction of the Large-Scale Structure*, *ApJ* **449** (1995) 446 [[astro-ph/9410080](#)].
- [20] U. Seljak, *Cosmography and power spectrum estimation: a unified approach*, *Astrophys. J.* **503** (1998) 492 [[astro-ph/9710269](#)].
- [21] W.H. Press, S.A. Teukolsky, W.T. Vetterling and B.P. Flannery, *Numerical Recipes 3rd Edition: The Art of Scientific Computing*, Cambridge University Press, USA, 3 ed. (2007).

- [22] B.D. Wandelt, D.L. Larson and A. Lakshminarayanan, *Global, exact cosmic microwave background data analysis using Gibbs sampling*, *Phys. Rev. D* **70** (2004) 083511 [[astro-ph/0310080](#)].
- [23] K.M. Smith, O. Zahn and O. Doré, *Detection of gravitational lensing in the cosmic microwave background*, *Phys. Rev. D* **76** (2007) 043510 [[0705.3980](#)].
- [24] F. Elsner and B.D. Wandelt, *Efficient Wiener filtering without preconditioning*, *A&A* **549** (2013) A111 [[1210.4931](#)].
- [25] D. Kodi Ramanah, G. Lavaux and B.D. Wandelt, *Wiener filter reloaded: fast signal reconstruction without preconditioning*, *MNRAS* **468** (2017) 1782 [[1702.08852](#)].
- [26] M.A. Aragon-Calvo, *Classifying the large-scale structure of the universe with deep neural networks*, *MNRAS* **484** (2019) 5771 [[1804.00816](#)].
- [27] M.A. Petroff, G.E. Addison, C.L. Bennett and J.L. Weiland, *Full-sky Cosmic Microwave Background Foreground Cleaning Using Machine Learning*, *ApJ* **903** (2020) 104 [[2004.11507](#)].
- [28] B. Costanza, C.G. Scóccola and M. Zaldarriaga, *Enhancing CMB map reconstruction and power spectrum estimation with convolutional neural networks*, *J. Cosmology Astropart. Phys.* **2024** (2024) 041 [[2312.09943](#)].
- [29] U. Seljak, G. Aslanyan, Y. Feng and C. Modi, *Towards optimal extraction of cosmological information from nonlinear data*, *J. Cosmology Astropart. Phys.* **2017** (2017) 009 [[1706.06645](#)].
- [30] B. Horowitz, U. Seljak and G. Aslanyan, *Efficient optimal reconstruction of linear fields and band-powers from cosmological data*, *J. Cosmology Astropart. Phys.* **2019** (2019) 035 [[1810.00503](#)].
- [31] E.F. Bunn, M. Zaldarriaga, M. Tegmark and A. de Oliveira-Costa, *E/B decomposition of finite pixelized CMB maps*, *Phys. Rev. D* **67** (2003) 023501 [[astro-ph/0207338](#)].
- [32] K.M. Smith and M. Zaldarriaga, *General solution to the E-B mixing problem*, *Phys. Rev. D* **76** (2007) 043001 [[astro-ph/0610059](#)].
- [33] S. Pal and R. Saha, *Reconstruction of full sky CMB E and B modes spectra removing E-to-B leakage from partial sky using deep learning*, *Journal of Astrophysics and Astronomy* **44** (2023) 84 [[2211.09112](#)].
- [34] E.F. Bunn and B. Wandelt, *Pure E and B polarization maps via Wiener filtering*, *Phys. Rev. D* **96** (2017) 043523 [[1610.03345](#)].
- [35] M. Münchmeyer and K.M. Smith, *Fast Wiener filtering of CMB maps with Neural Networks*, *arXiv e-prints* (2019) arXiv:1905.05846 [[1905.05846](#)].
- [36] D. Alonso, J. Sanchez, A. Slosar and LSST Dark Energy Science Collaboration, *A unified pseudo- C_ℓ framework*, *MNRAS* **484** (2019) 4127 [[1809.09603](#)].
- [37] O. Ronneberger, P. Fischer and T. Brox, *U-Net: Convolutional Networks for Biomedical Image Segmentation*, *arXiv e-prints* (2015) arXiv:1505.04597 [[1505.04597](#)].
- [38] A. Lewis, A. Challinor and A. Lasenby, *Efficient Computation of Cosmic Microwave Background Anisotropies in Closed Friedmann-Robertson-Walker Models*, *ApJ* **538** (2000) 473 [[astro-ph/9911177](#)].
- [39] Planck Collaboration, P.A.R. Ade, N. Aghanim, C. Armitage-Caplan, M. Arnaud, M. Ashdown et al., *Planck 2013 results. XVI. Cosmological parameters*, *A&A* **571** (2014) A16 [[1303.5076](#)].
- [40] A. Kogut, D.N. Spergel, C. Barnes, C.L. Bennett, M. Halpern, G. Hinshaw et al., *First-year wilkinson microwave anisotropy probe (wmap)* observations: Temperature-polarization correlation*, *The Astrophysical Journal Supplement Series* **148** (2003) 161.

- [41] A. Dosovitskiy, L. Beyer, A. Kolesnikov, D. Weissenborn, X. Zhai, T. Unterthiner et al., *An Image is Worth 16x16 Words: Transformers for Image Recognition at Scale*, *arXiv e-prints* (2020) [arXiv:2010.11929](https://arxiv.org/abs/2010.11929) [[2010.11929](https://arxiv.org/abs/2010.11929)].
- [42] K. Chen, *Matrix Preconditioning Techniques and Applications*, Cambridge Monographs on Applied and Computational Mathematics, Cambridge University Press (2005).
- [43] M. Kamionkowski, A. Kosowsky and A. Stebbins, *Statistics of cosmic microwave background polarization*, *Phys. Rev. D* **55** (1997) 7368 [[astro-ph/9611125](https://arxiv.org/abs/astro-ph/9611125)].
- [44] W. Hu, *Weak lensing of the CMB: A harmonic approach*, *Phys. Rev. D* **62** (2000) 043007 [[astro-ph/0001303](https://arxiv.org/abs/astro-ph/0001303)].
- [45] M.B. Costanza, C.G. Scóccola and M. Zaldarriaga, *Wiener Filter for cosmic microwave background maps using neural networks*, *Boletín de la Asociación Argentina de Astronomía La Plata Argentina* **64** (2023) 193.